Combined κ-carbide precipitation and recovery enables ultra-high strength and ductility in light-weight steels

Frederike Brasche[*,1], Christian Haase[2], Marta Lipińska-Chwałek[3,4], Joachim Mayer[3,4], Dmitri A. Molodov[1]

[1]*Institute for Physical Metallurgy and Metal Physics, RWTH Aachen University, 52074 Aachen, Germany, brasche@imm.rwth-aachen.de*

[2]*Steel Institute, RWTH Aachen University, 52072 Aachen, Germany*

[3] *Ernst Ruska-Centre for Microscopy and Spectroscopy with Electrons, Forschungszentrum Jülich GmbH, 52425 Jülich, Germany*

[4] *Central Facility for Electron Microscopy, RWTH Aachen University, 52074 Aachen, Germany*

Abstract

Light-weight high-manganese steels with high aluminium and carbon contents are known to possess high age-hardening potential due to the precipitation of nano-sized κ-carbides. Although in recrystallized material the precipitation of the κ-phase has been widely researched, the influence of pre-deformation/deformation microstructure on the formation of κ-carbides is still unknown. The present study aims at gaining an increased understanding of the underlying mechanisms (and their interplay) active during annealing after pre-deformation, i.e. concurrent strengthening by precipitation of κ-carbides and softening by recovery/recrystallization. Therefore, a Fe-29.8Mn-7.65Al-1.11C steel was age-hardened in deformed/cold-rolled as well as in recrystallized condition. The microstructure and tensile behaviour of the material in both states after annealing treatments at 600-800 °C were investigated by means of light optical microscopy, (high-resolution) scanning transmission electron microscopy, x-ray diffraction and hardness measurements as well as tensile tests. The focus was put on understanding the interplay between microstructural defects (e.g. dislocations), precipitation of κ-carbides, and recovery/recrystallization. The fundamental dependence of strengthening and softening mechanisms on the precondition, annealing parameters and correlation with the mechanical properties are discussed.

Key words: Light-weight steel; κ-carbide; microstructure; texture; recovery; mechanical properties

*Corresponding author. Tel.: +49 241 8026864, fax: +49 241 8022301. E-mail address: *brasche@imm.rwth-aachen.de* (Frederike Brasche).

1. Introduction

In the past decades, Fe-Mn-Al-C alloys with high aluminium content have been subject of extensive studies due to their potential to provide a combination of outstanding mechanical properties with reduced mass density [1-5]. Having good fatigue properties [6, 7] and a good oxidation resistance at elevated temperatures [8, 9], this alloy class already fulfils most requirements for structural parts for the automotive industry. However, a high crash worthiness, which is essential for various parts of the body-in-white, requires precise adjustment of the mechanical properties, i.e. yield strength, work-hardening behaviour, and ductility. This can be achieved by designing the microstructure of light-weight high-manganese steels (HMnS) with respect to its individual microstructural constituents, such as dislocations, grain boundaries, precipitates and interfaces.

Alloying of HMnS with more than 7 wt% aluminium and more than 0.7 wt% carbon [10, 11] not only leads to a significant reduction of the alloy mass density by 1.3-1.5% per 1 wt% aluminium [5, 12]. It additionally results in the precipitation of chemically ordered κ-carbides with an ideal stoichiometry of $(Fe,Mn)_3AlC$, characterised by the cubic $L1_2$ structure, with aluminium atoms located at the cube corners, iron or manganese at the face-centered sites and carbon at the body-centered octahedral site. A frequently reported off-stoichiometry of the κ-carbides, in the sense of carbon deficiency, resulted in the more common notation $(Fe,Mn)_3AlC_x$ ($x<1$) [13-15]. Depending on the cooling rate after homogenization or isothermal annealing, as well as on the temperature and duration of aging, κ-carbides precipitate inter- and/or intragranular. At low aging temperatures (450-650 °C), intragranular κ-carbides are reported to form, whereas at temperatures between 650 and 800 °C also intergranular κ-carbides were found [10]. Intragranular κ-carbides precipitate uniformly distributed throughout the grains of the austenitic matrix, by a sequence of spinodal decomposition of the high temperature austenite, a short-range ordering (SRO) reaction transforming the solute-rich austenite into an $L1_2$ phase, and final reordering of carbon to form κ-carbides with an $E2_1$ structure [16-19]. Due to the small lattice mismatch of less than 3%, these κ-carbides are coherently embedded in the austenitic matrix showing a cube-on-cube relationship with the austenite, i.e. $\langle 100\rangle_\kappa \| \langle 100\rangle_\gamma$ and $\{100\}_\kappa \| \{100\}_\gamma$ [17, 20, 21]. Intergranular κ-carbides precipitate as coarse particles heterogeneously distributed at grain boundaries, either by a precipitation reaction, cellular transformation or eutectoid reaction [22]. Apart from the light-weight HMnS consisting of an austenitic matrix with SRO clusters or κ-carbides, triplex (austenite+ferrite+κ-carbides) steels have been widely discussed [23-25]. However, the current study focusses solely on dual-phase (austenite+κ-carbide) steels.

Due to the strong increase of the stacking fault energy (SFE) by alloying HMnS with aluminium and carbon, strain-induced phase transformation and mechanical twinning (as known from HMnS with

SFE less than 40 mJ/m^2 [26]) are suppressed. Unlike expected for a material with high SFE, wavy glide was not observed in light-weight HMnS. In the austenitic phase, planar glide of dislocations was found to occur [2, 4, 12, 27-30]. The reason for the appearance of planar slip has been controversially discussed in the past. According to the majority of the studies, the presence of SRO clusters and/or intragranular κ-carbides promotes the planar glide of dislocations. More precisely, a dislocation cutting through an ordered κ-carbide (or an SRO cluster) leaves an antiphase boundary behind, which can be restored by a trailing dislocation. Therefore, glide plane softening of this specific glide plane occurs for the succeeding dislocations, resulting in planar glide [2-4, 12, 27, 31, 32]. Planar glide of dislocations strongly influences the strain-hardening behaviour of light-weight HMnS. Several concepts have been proposed for materials with SRO clusters and/or κ-carbides to explain the strong strain hardening up to relatively high strain levels. The MicroBand-Induced Plasticity (MBIP) effect is characterized by planar glide of dislocations causing the formation of a Taylor lattice at low strains. Upon further straining the microstructure is gradually refined by the formation and intersection of domain boundaries (DBs) and microbands (MBs), which results in a pronounced strain hardening. MBs are formed during deformation by parallel DBs with short separation distance. Since these MB are misoriented with respect to the surrounding grains, they facilitate further strain accommodation by providing newly oriented material [27, 33]. Welsch et al. [4] stated that formation and subdivision of a crystallographically aligned slip band structure is rather responsible for the strong strain hardening and related the inverse average slip band distance to the strength contribution. Haase et al. [2] reported similar results and introduced the term “slip band refinement-induced plasticity (SRIP)” for the occurring deformation mechanism. The influence of ageing on the mechanical properties was, amongst others, investigated by Choi et al. [34], who reported a decreasing strain hardening rate with increasing ageing time (3 h, 10 h, 192 h), due to an increasing slip band distance. In Refs. [12, 35, 36] a strong age-hardening effect due to precipitation of intragranular κ-carbides was reported for Fe-30Mn-1.2C-xAl steels with varying aluminium content, when x is higher than 8 wt%.

The precipitation kinetics of κ-carbides in recrystallized material was reported to follow a typical age hardening characteristic, where the peak hardness increases at lower annealing temperatures, but is then achieved at longer aging times [20]. The peak hardness was reported to occur along with a decrease in tensile elongation, attributed to the appearance of coarse intergranular κ-carbides [37-40]. Since SRO clusters (that act as nuclei for the κ-carbide precipitation) or even nano-sized κ-carbides are already present after water quenching from homogenization temperature, the aging kinetics are assumed to proceed very fast at the early stage of annealing [3, 4].

As stated in the previous paragraphs, the morphology and precipitation kinetics of κ-carbides, as well as the deformation behaviour of HMnS, are fairly well understood in the case of recrystallized material. However, precise design of the microstructure for an application-dedicated adjustment of the mechanical properties also requires comprehensive knowledge of the material behaviour in the

deformed state subjected to heat treatment. In particular, the underlying precipitation, recovery, and recrystallization mechanisms, as well as their interplay during thermo-mechanical treatment of deformed material need to be understood. Therefore, the approach applied in the present study employs heat treatment of a single-phase austenitic light-weight HMnS in the cold-rolled state, which activates concurrent softening and strengthening mechanisms. In the selected temperature range, κ-carbide precipitation (causing hardening) as well as recovery/recrystallization (causing softening) occur. Since dislocation and grain boundary movement are strongly influenced by intra- and intergranular carbides, the interaction of these needs to be investigated and understood in order to precisely design the microstructure by heat treatment. The aim of the present study was to gain a profound understanding of the mechanisms underlying the concurrent softening and strengthening processes, and manipulate these processes to control the mechanical properties. A Fe-29.8Mn-7.65Al-1.11C light-weight steel was examined by applying heat treatments with various parameters and analysing the precipitation morphology and kinetics as well as recovery and recrystallization behaviour by means of hardness measurements, light optical microscopy (LOM), (high-resolution) scanning transmission electron microscopy ((HR)STEM)), and x-ray diffraction (XRD) measurements. The fact, that softening and hardening mechanisms can be combined in one annealing treatment, enables for short processing routes and manifests the potential for industrial application. Consequently, tensile tests and fracture surface analysis were performed to provide information about the resulting mechanical behaviour and applicability of the processing route.

2. Experimental

2.1 Material and processing

A single-phase austenitic light-weight steel with age-hardening potential was required for the dual-stage heat treatment as described in section 1. Therefore, the chemical composition presented in Table 1 was investigated. Fig. 1 shows the phase fraction-temperature diagram for chemical composition of the alloy. The respective SFE value of the alloy (Table 1) was calculated with a subregular solution thermodynamic model [41, 42].

Table 1. Chemical composition and stacking fault energy value of the investigated steel.

Element	Fe	C	Mn	Al	Si	SFE (mJ/m^2)
(wt%)	bal.	1.11	29.8	7.65	0.09	85

The investigated steel was strip cast and subsequently homogenized at 1150 °C for 5 h. All heat treatments in the present study were carried out under Ar atmosphere and followed by water quenching. Remaining inhomogeneities, especially in the grain size distribution, were eliminated by cold rolling to 30% thickness reduction and subsequent recrystallization at 900 °C for 1 h. Eventually, cold rolling to 50% thickness reduction followed by recrystallization at 800 °C for 1 h provided the two initial material states for the present study, i.e. cold rolled (CR) and recrystallized (RX). Final annealing treatments at temperatures between 600-800 °C (indicated in Fig. 1 with a red-shadowed area) were applied to both initial states, in order to investigate the influence of a defect structure (in the CR material) on the precipitation of κ-carbides and on the recovery/recrystallization behaviour.

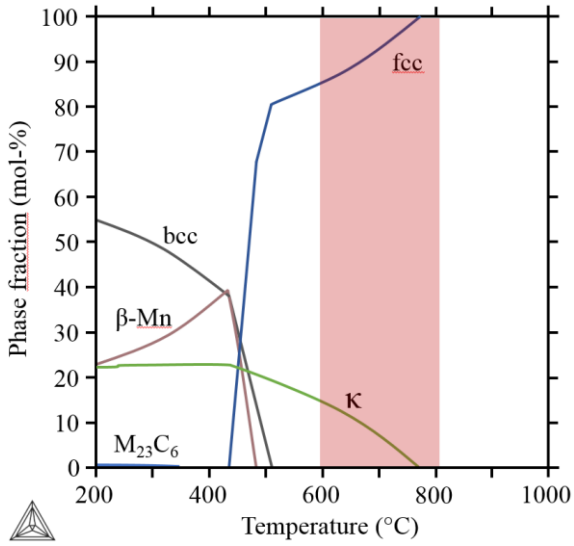

Fig. 1. Equilibrium phase fractions as a function of temperature for the investigated steel (based on [2]). The temperature range in which the final heat treatment was carried out is marked in red.

2.2 Sample preparation and characterization

Specimens with the dimension of 10 mm x 12 mm (transverse direction (TD) × rolling direction (RD)) were cut from the rolled sheets by electrical discharge machining. TEM, STEM, hardness and texture measurements were carried out on the middle layer of the RD-TD cross-section, whereas light optical micrographs were taken on the RD-ND (ND: normal direction) cross-section. All specimens were mechanically ground with SiC grinding paper up to 4000 grit and mechanically polished using 3 and 1 μm diamond suspension. Subsequent electropolishing, performed at room temperature and 22 V with an electrolyte consisting of 700 ml ethanol (C_2H_5OH), 100 ml butyl glycol ($C_6H_{14}O_2$), and 78 ml perchloric acid (60%) ($HClO_4$), provided a deformation-free surface for hardness (electropolishing for 20 s) and texture measurements (electropolishing for 2 min). The microstructure was visualized for optical microscopy after 20 s electropolishing by etching in a modified Klemm-solution (300 ml H_2O, 20 g $Na_2S_2O_3$) with 2 g potassium disulfide ($K_2S_2O_2$) for 5-10 s. (S)TEM specimens were prepared by mechanical grinding, down to 100 μm thin sheets. Subsequently, disks with a diameter of 3 mm were stamped out and twin-jet electropolished at -30 °C using an electrolyte consisting of 5% perchloric acid ($HClO_4$) and 95% methanol (CH_3OH).

Electron-transparent TEM samples were investigated with the aid of conventional TEM techniques using a FEI Tecnai F20 [43]. The HR imaging of the material structure was performed with a FEI Titan G2 80–200 Cs probe-corrected STEM [44], operated at 200 kV. STEM imaging was additionally carried out in a Dual-Beam focused ion beam (FIB) FEI Helios Nanolab 600i and optical micrographs were acquired with a Zeiss Axio Vision.

The mechanical behaviour was investigated by hardness measurements using a Shimadzu HMV microhardness tester with a load of 1 kg (HV1) taking ten indents per specimen and uniaxial tensile tests carried out perpendicular to RD with a constant strain rate of 10^{-3} s^{-1} in a Zwick 100 mechanical testing device. Three flat bar tensile specimens with a gauge length of 30 mm, gauge width of 6 mm, fillet radius of 20 mm and a total length of 124 mm, were examined for each material condition.

The macro-texture was measured in a Bruker D8 Advance X-ray diffractometer with a HI-STAR area detector operated at 30 kV and 25 mA, obtaining three incomplete (0-85°) {111}-, {200}-, and {220}-pole figures. The corresponding orientation distribution functions (ODFs) were calculated utilizing the MATLAB®-based MTEX toolbox [45, 46]. In order to compare the texture intensities of different material states, the texture index (TI) was used and calculated as follows:

$$\int f(g)^2 dg \tag{1}$$

where f(g) represents the ODF of the orientations g given by Euler angles.

3. Results

3.1 Microstructure of the initial material states

The microstructure of both initial states of the investigated alloy are presented in Fig. 2 with the aid of LOM image and EBSD band contrast mapping for CR and RX, respectively. The CR material was characterized by flattened grains, which were elongated in the rolling direction. Also a few shear bands were observed (indicated exemplarily in Fig.1a with arrows). The RX material consisted of globular grains including annealing twin boundaries with an average grain size of 5 µm (grain size determined by considering twin boundaries as grain boundaries).

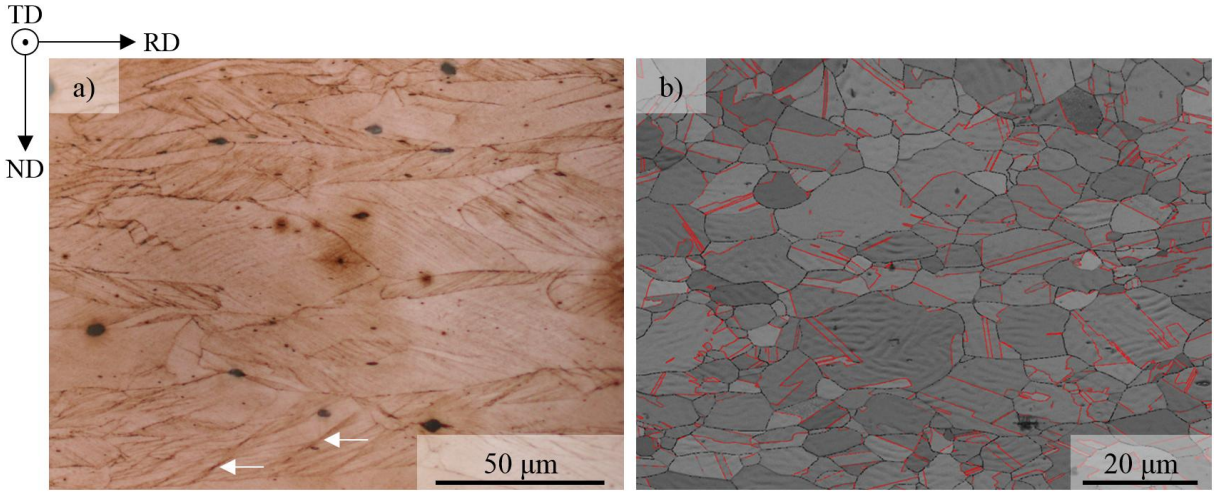

Fig. 2. Micropgraphs of the two initial conditions: a) LOM micrograph of the CR material and b) EBSD band-contrast mapping of the RX material. Red lines denote Σ3 (60°<111>) grain boundaries, white arrows indicate shear bands.

3.2 Hardness evolution

The hardness evolution of the material annealed at 600-700 °C is presented in Fig. 3 as a function of annealing time. The initial material states exhibited hardness values of 440 (CR) and 268 HV1 (RX), respectively. The CR material subjected to annealing at 600 and 650 °C showed, in both cases, a peak hardness at short annealing time of 10 min, followed by a continuous hardness decrease. After 4 h of annealing, slightly lower (428 HV1) and significantly lower (379 HV) hardness values were reached for CR material annealed at 600 and 650 °C, respectively, which correspond to 3% and 14% hardness deterioration, as compared to the CR state. Annealing at 700 °C resulted in a strong (33%) decrease of hardness within the initial 20 min of annealing. Apart from a slight hardness increase observed after 1h annealing time, the hardness remained at the level obtained after 20 min of annealing. Annealing of the RX material resulted in a substantial increase of the hardness values within first hour of annealing. The increase in hardness values was inversely proportional to the applied annealing temperature, with

the highest values of about 370 HV1 obtained for the material annealed at 600 °C, corresponding to 38% increase with respect to the initial RX material hardness. After a long annealing time (between 1 and 4 h) the hardness of the RX material remained at an almost constant level (for each applied annealing temperature).

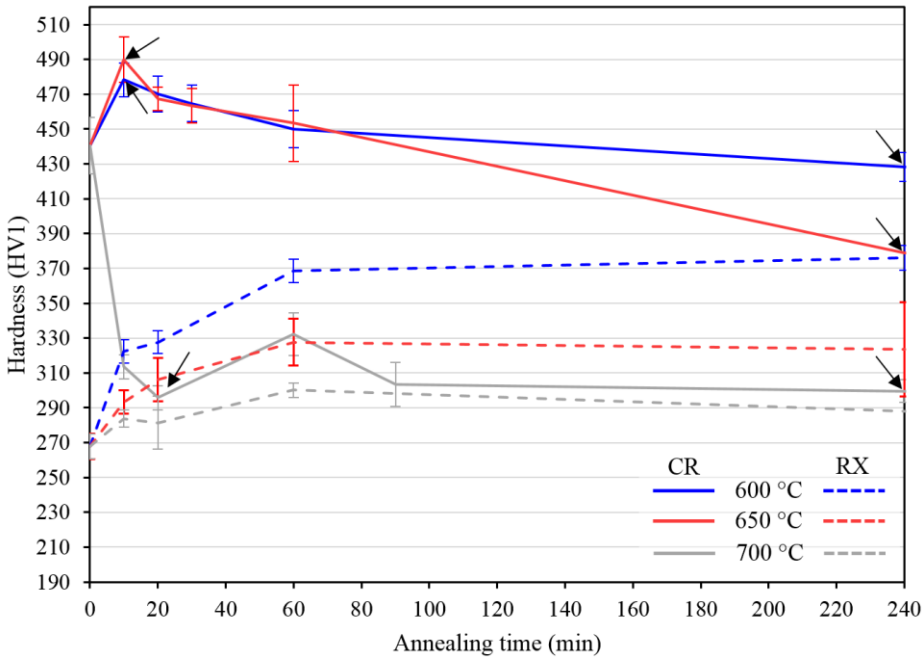

Fig. 3. Hardness evolution as a function of annealing time for the material in the two initial conditions CR (solid lines) and RX (dashed lines) annealed at 600, 650 and 700 °C. The material states investigated in detail in the following paragraphs are marked with black arrows. The corresponding micrographs are illustrated in Figs. 4 and 5).

3.3 Microscopy

The material conditions marked in the hardness curve in Fig. 3 with black arrows were selected for microstructural analysis by LOM (Fig. 4) and TEM (Fig. 5). The onset of recrystallization could not be observed during annealing at 600 °C (Fig 4a and b). At 650 °C the first small recrystallization nuclei were present after annealing for 240 min along grain boundaries and at triple points (Fig 4d). At a higher temperature (700 °C) a partially recrystallized microstructure was formed after 20 min. Annealing for 240 min at 700 °C did, however, still not lead to full recrystallization. For all annealing temperatures, after 240 min the grain boundaries were decorated with large intergranular κ-carbides.

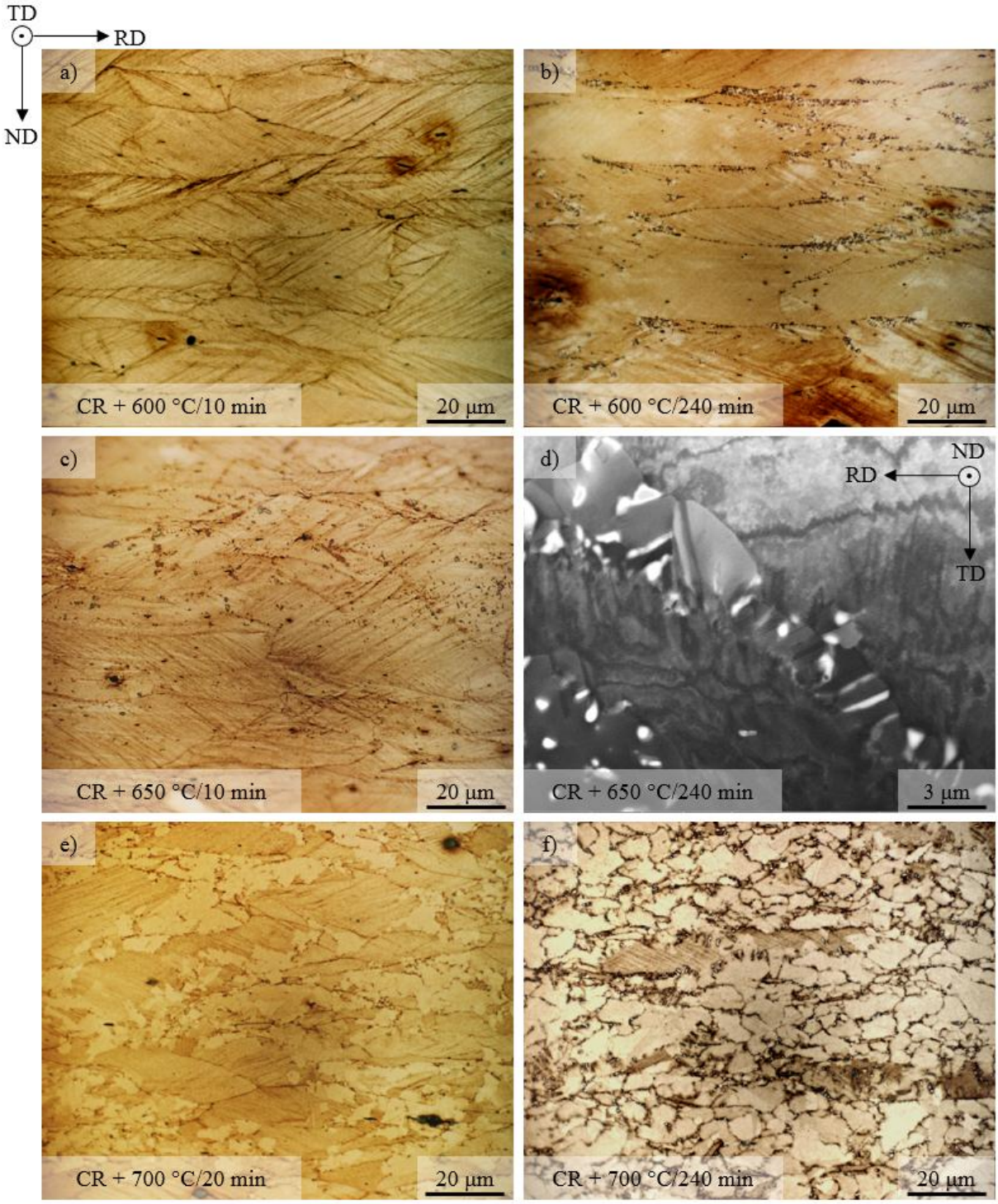

Fig. 4. LOM (a-c, e, f) and STEM (d) micrographs of the CR material annealed at 600 (a, b), 650 (c, d), and 700 °C (e, f). Images of the microstructures obtained after short annealing times of 10 or 20 min are presented in the left column, whereas those obtained after a long annealing time of 240 min are shown in the right column. Note the difference in the relative orientation of the specimens in a, b, c, e and f (the same for all LOM images) and d (STEM) micrograph.

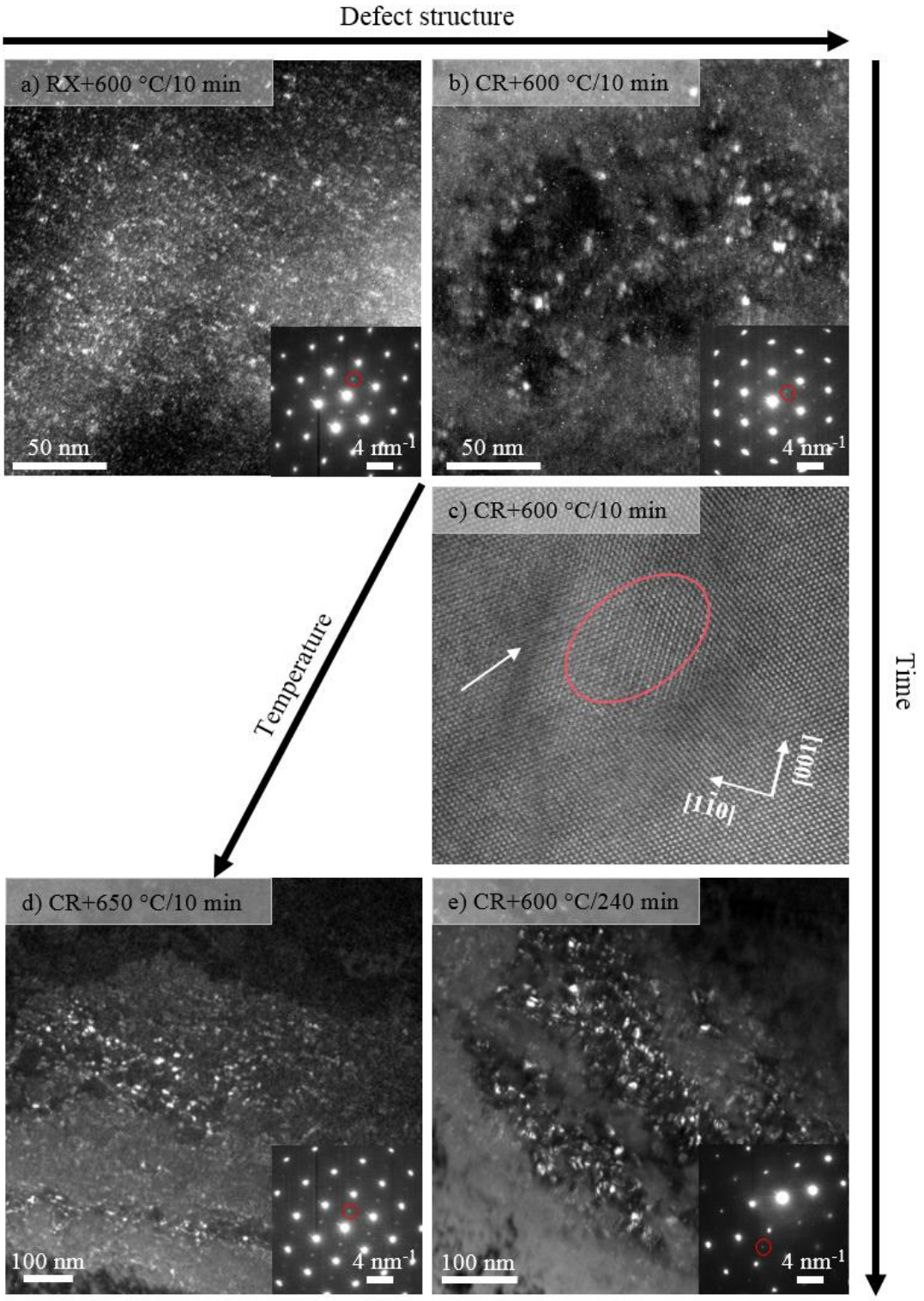

Fig. 5. TEM images of the microstructures observed in RX (a) and CR (b-d) material after annealing treatments at 600 °C for 10 min (a-c), 650 °C for 10 min (d) and 600 °C for 240 min (e). DF TEM images (a, b, d and e) and the corresponding SADPs (insets) acquired in the orientations close to [110] zone axis. Intensities of DF images correspond to the κ-phase super lattice reflections g_κ=(001) in (a-d) and g_κ=(003) in (e), indicated in SADPs with red circles. HR HAADF STEM (c) acquired in the [110] zone axis orientation: red ellipse - encloses κ-carbide precipitate, localized in the vicinity of defects (blurry shadows indicated with white arrow), inset with white vectors - depicts crystallographic directions in the HR image.

Fig. 5 shows (S)TEM images of the microstructures observed in RX and CR materials after the respective annealing treatments. K-Carbides appear in the dark-field (DF) TEM images as bright precipitates, as the images were acquired with the intensities of the κ-carbide super lattice reflections. The corresponding selected area diffraction patterns (SADP) revealed crystallographic orientations of the imaged microstructures. Intragranular κ-carbides were present in the microstructure already after a short annealing time of 10 min in the RX (Fig. 5a) as well as in the CR material (Fig. 5b). κ-Carbides observed in the RX material annealed for 10 min at 600 °C were very small (≤1 nm in diameter) and evenly distributed throughout the grains of the austenitic matrix. The complex defect structure of the CR material resulted, upon annealing, in the precipitation of significantly larger κ-carbides, irregular in size and spatial distribution. The largest precipitates (ca. 7 nm in diameter) localized at defects. The atomic-resolution appearance of the microstructure representative for the CR material annealed for 10 min at 600 °C is presented in Fig. 5c, by means of HR high-angle annular dark-field (HAADF) STEM (acquired in the [110] sample orientation, i.e. beam direction parallel to [110] crystallographic direction of the sample). A κ-carbide precipitate, of ca. 7 nm in size (indicated with red ellipse), is located at the structural defect of the austenitic matrix (darker blurred-line shape, with deteriorated atomic resolution - indicated in Fig. 5c with a white arrow). The atomic structure of the chemically ordered κ-carbide can be distinguished from chemically disordered matrix as a structure region with $(1\bar{1}0)$ planes exhibiting alternating higher and lower brightness (see vectors of crystallographic directions indicated in Fig. 5c). Due to the high sensitivity of the HAADF images to the atomic weight (Z) and an alternating fill-up of the $(1\bar{1}0)$ crystal planes in the κ-carbide (observed along [110] direction) with heavier (Fe and Mn) and lighter (Al) atoms, the alternating atomic planes of brighter (heavier atoms) and darker (lighter atoms) appearance are observed along $[1\bar{1}0]$ direction within the area of the κ-carbide. Neither a longer annealing time (240 min at 600 °C, Fig. 5d) nor a higher annealing temperature (650 °C for 10 min, Fig. 5e) had a significant influence on distribution or morphology of the κ-carbides in CR material. For both mentioned annealing conditions, comparable precipitate structures were obtained in the CR material, with a slightly increased size of κ-precipitates (the largest diameter of carbides did not exceed 15 nm in either material states).

3.4 Texture evolution

The results from macro texture analysis of specific material conditions are illustrated in Fig. 6 by means of φ_2=45° ODF sections and texture indices. The CR material exhibited an equally high intensity of orientations along the α-fiber ({110}<100> Goss and {110}<112> Brass) and the {112}<111> Cu texture component. During annealing at 600 °C, the texture remained unchanged up until an annealing time of 240 min and annealing at 650 °C caused a very slight weakening of the texture. In contrast, the heat treatment at 700 °C resulted in significant weakening of the texture, particularly of the Cu texture component. The texture index decreased from 3.54 in the CR condition to 1.22 after 240 min annealing.

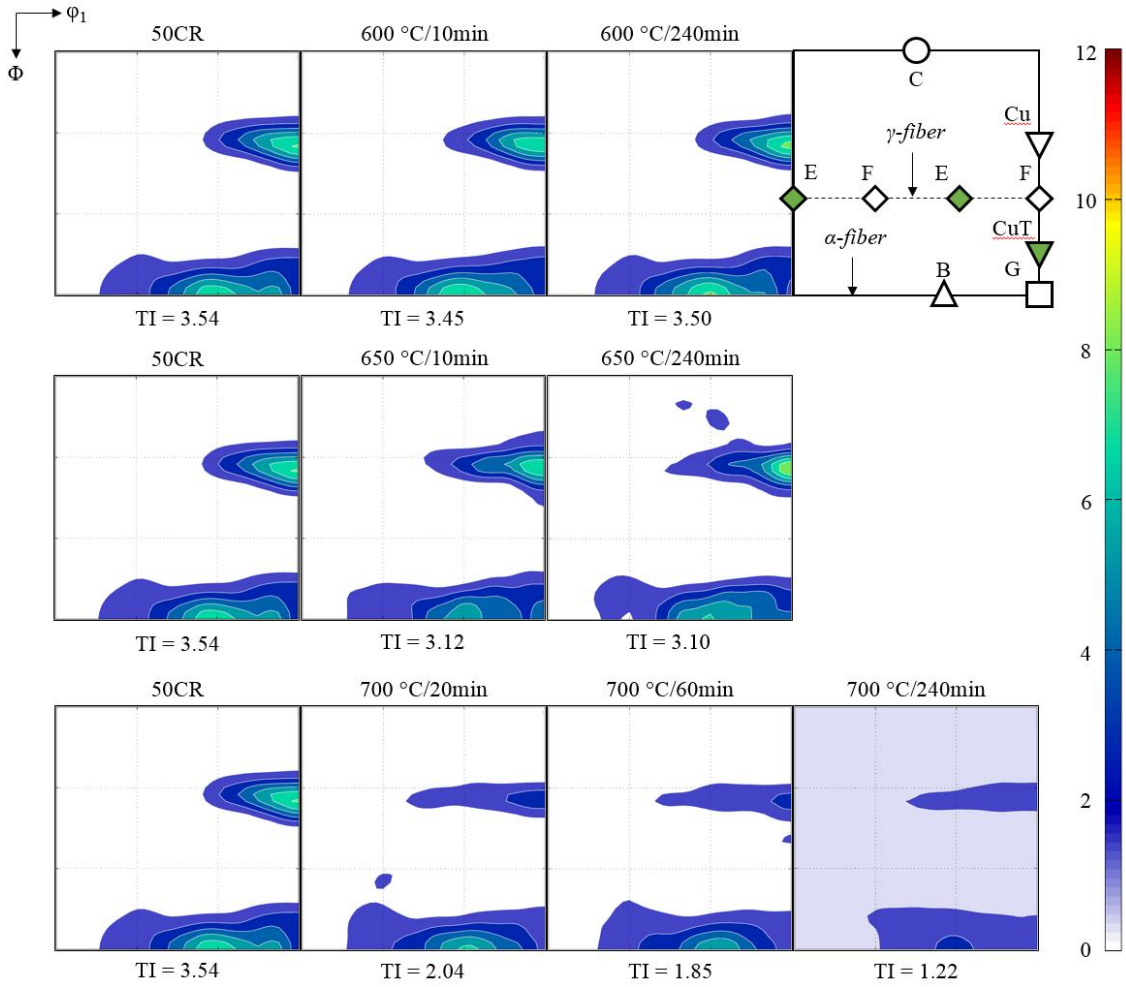

Fig. 6. Texture (ODF sections at φ2=45°) of the CR material annealed at 600 °C and 650 °C for 10 and 240 min, as well as annealed at 700 °C for 20, 60, and 240 min. A schematic of the ideal positions of the rolling texture components is illustrated in the upper right corner. The corresponding declaration of the texture components can be found in Ref. [47].

3.5 Tensile tests

In addition to hardness testing, the mechanical behaviour of the material in the selected annealing conditions was examined by uniaxial tensile tests at room temperature. The resulting engineering stress-engineering strain curves and mechanical properties are illustrated in Fig. 7. The CR material was compared to states after a short (10 min), intermediate (30 min) and long (240 min) annealing time at 600 °C. The material exhibited a yield strength ($\sigma_{0.2}$) of 1457 MPa in the CR state, which slightly decreased with increasing annealing time (1429 MPa after 240 min). After 10 min annealing the elongation to fracture (ε_f) increased from 3.4% in the CR state to 7.0%. Longer annealing treatments resulted in a decreased ductility to 3.1% after 30 min and 4.7% after 240 min annealing. In order to investigate the influence of temperature on the mechanical behaviour, tensile tests were additionally performed on the material annealed at 650 °C for 30 min. In this case, the yield strength decreased by 213 MPa, to 1244 MPa as compared to the CR material, whereas the ductility remained at a similar level (Fig. 7).

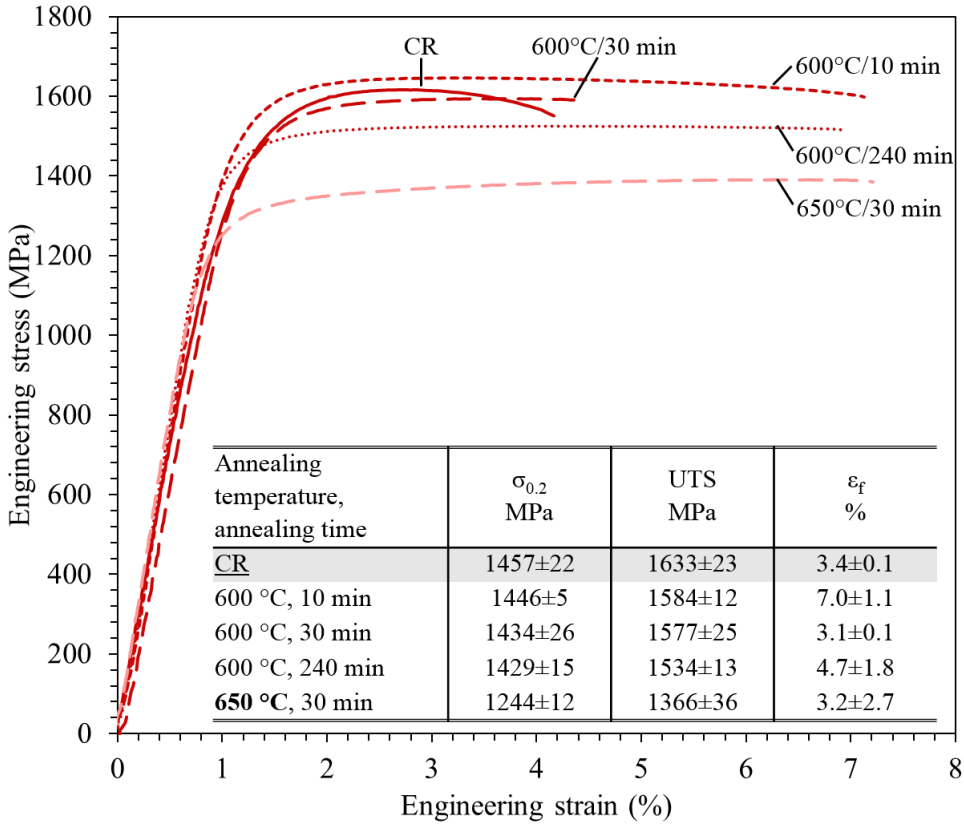

Annealing temperature, annealing time	$\sigma_{0.2}$ MPa	UTS MPa	ε_f %
CR	1457±22	1633±23	3.4±0.1
600 °C, 10 min	1446±5	1584±12	7.0±1.1
600 °C, 30 min	1434±26	1577±25	3.1±0.1
600 °C, 240 min	1429±15	1534±13	4.7±1.8
650 °C, 30 min	1244±12	1366±36	3.2±2.7

Fig. 7. Engineering stress – engineering strain curves and mechanical properties of the investigated material cold rolled to 50% thickness reduction and annealed at 600 and 650 °C for various annealing times.

Fig. 8 displays fracture surfaces (secondary electron (SE) micrographs) of tensile test specimens of the CR material annealed at 600 °C and 650 °C for various annealing times. The fracture surface of the CR material was characterized by dimples with diameters of 1-5 μm and flat areas of quasi-brittle fracture, located at elliptical voids. With increasing annealing time, the area fraction consisting of dimples significantly decreased and large, cleavage-like facets in the shape of deformed grains (cf. Fig. 2) evolved. These facets revealed three characteristic features, which are marked in Fig. 8e: (1) spherical voids of different size (blue arrows), (2) linear markings extending either along one or two different directions within one grain (red lines), and (3) nodules, which frequently decorated such markings (white arrow). After 30 min annealing and beyond, the area containing dimples approached an insignificantly small fraction. By increasing the temperature to 650 °C (fig. 8e), the facets including voids, linear markings, and nodules were still present, although their number was noticeably smaller, as compared to the material annealed at 600 °C (both after annealing for 30 min).

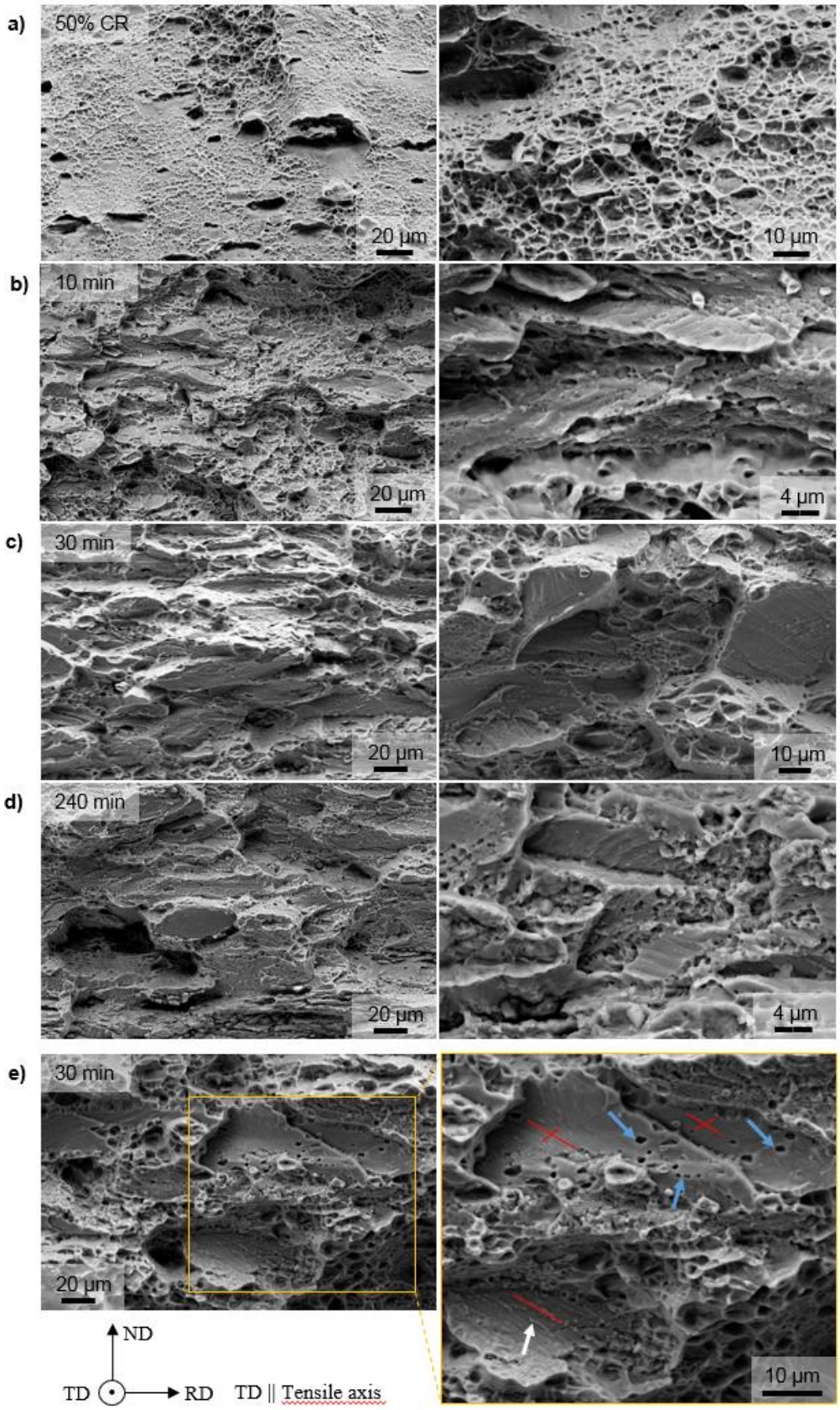

Fig. 8. SE images of the fracture surfaces of tensile test specimens of the CR material in the initial state (a) and after various annealing times at 600 °C (b-d) and 650 °C (e). Images in the left column give an overview of the fracture surface, whereas images in the right column provide a magnified view. In the inset of e) characteristic features on facets found in the materials fracture surfaces are highlighted. Blue arrow: spherical voids, red lines: linear markings, white arrow: nodules.

4. Discussion

A Fe-29.8Mn-7.65Al-1.11C light-weight steel in two initial microstructural states, namely CR and RX, has been subjected to various aging treatments in order to investigate the influence of a deformation substructure on the precipitation kinetics and morphology of κ-carbides. Different precipitation states and recovered or (partially) recrystallized microstructures were formed and comprehensively investigated to gain knowledge about the interplay between concurrently occurring softening (recovery/recrystallization) and hardening (κ-carbide precipitation) during the annealing treatment. In the following sections, the obtained results will be discussed with respect to the potential of the dual-phase annealing treatment for the precise design of the microstructure in order to improve mechanical properties

4.1 Precipitation behaviour

Several studies have been carried out on material with a similar chemical composition as that of the present alloy [2-4, 15, 40, 48, 49]. From these studies, the precipitation kinetics and morphology of the κ-carbides precipitated in fully recrystallized material are known and have been similarly observed in the RX material of the material investigated in the present study. The κ-carbides (or their nuclei) are reported to exist already after quenching in the form of long-range ordered clusters [4]. After dedicated aging, fine evenly distributed cuboidal and plate-like κ-carbides precipitate in the austenitic matrix in a defined crystallographic relation ($\{001\}_\kappa||\{001\}_\gamma$). Due to orientation of the κ/γ interfaces along elastically soft ⟨001⟩ directions of κ-carbides [2, 3] and a lattice mismatch of less than 3%, a coherent phase boundary between the two phases is formed [40]. However, the influence of the defect structure in the austenite on the precipitation behaviour of κ-carbides has not been systematically investigated so far, but it is important when designing a thermo-mechanical treatment to improve the mechanical properties. The current experiments revealed two major differences in the morphology and distribution of the κ-carbides precipitating in recrystallized and deformed material. Namely, a complex defect structure as obtained after cold rolling of the material led to:

- precipitation of significantly larger intragranular κ-carbides with irregular size
- preferential precipitation at defects rather than a homogeneous distribution in the bulk.

The widely accepted concept of the κ-carbide formation describes their precipitation as a sequence of spinodal decomposition, short-range ordering and reordering of carbon [16-19]. The diffusion of solutes, which is necessary for spinodal decomposition, is much faster along dislocation cores than in the defect-free bulk. It can therefore occur over longer spatial ranges within a given time [50]. According to our assessment, the enhanced diffusion and strong (elastic) lattice distortions present in the deformed material account for the spinodal decomposition into the solute-lean (C and/or Al) and the solute-rich phase to occur in a larger spatial volume as compared to the recrystallized material (cf. Fig. 9). Consequently, the local volume in the vicinity of defects, which is enriched in Al and C, is

larger than in the defect-free bulk. The subsequent short-range ordering and reordering of carbon take place in these relatively larger volumes and resulted in the formation of significantly larger κ-carbides (corresponding to the size of the volume enriched in C and Al). Accordingly, the deformed material provides, for the same annealing duration, significantly larger κ-carbides, but of more irregular size and spatial distribution (resulting from the inhomogeneity in defect distribution) than the recrystallized material.

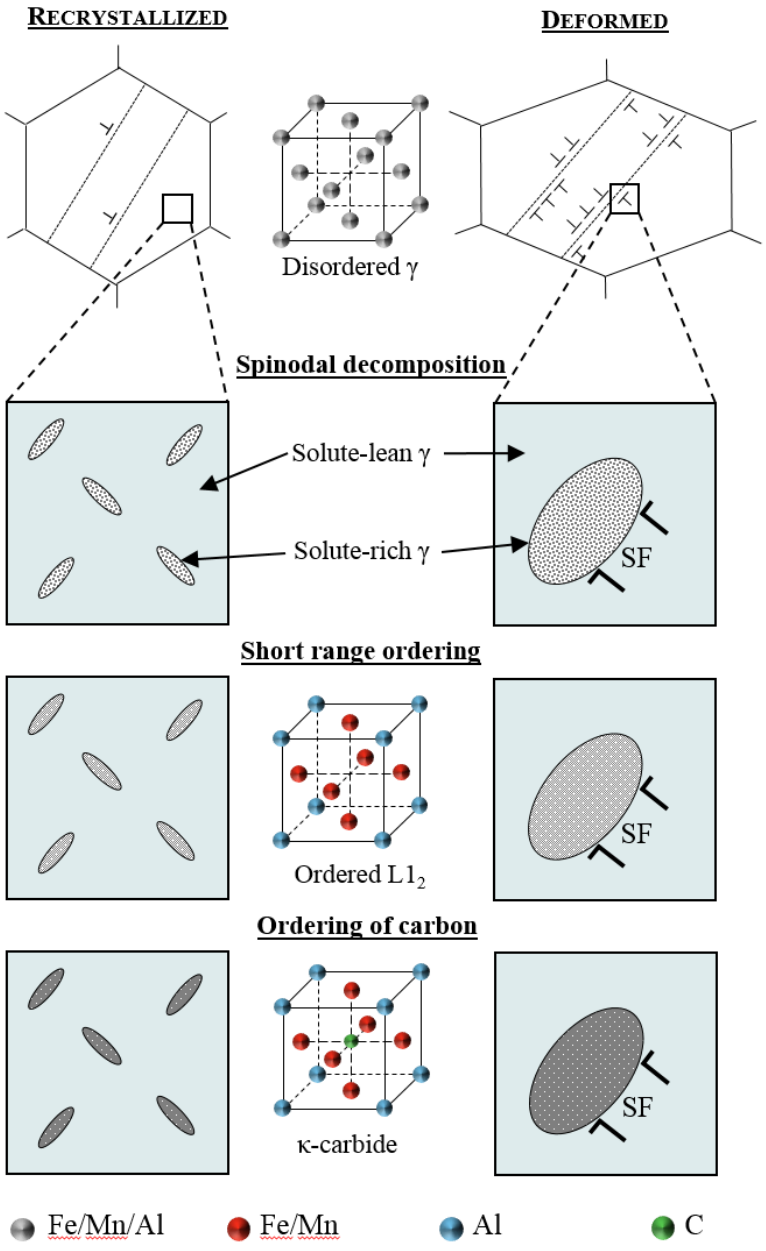

Fig. 9. Schematic of the precipitation mechanism of κ-carbides in recrystallized (left column) and deformed material (right column). SF denotes a stacking fault.

The parameter, which was reported to restrict the growth of κ-carbides, is mainly the coherency strain [49]. As described above (Sec. 3.3), the phase boundaries between the austenitic matrix and κ-carbides formed in the CR state (as also in the RX state) were coherent, albeit the large size of the κ-carbides in

the deformed state. Ultimately, the equilibrium size of the formed κ-carbides is therefore still defined by the concurrent appearance of coherency strains on the one hand and chemical driving force of ordering on the other hand. However, due to the faster diffusion along dislocation cores, the nuclei for κ-carbide-formation are larger. This interpretation is supported by the finding that no significant growth of intragranular κ-carbides has occurred neither in the current (cf. Fig. 5) nor in previous studies [49]. A larger size of precipitates in the deformed material compared to the recrystallized material and distinct (inhomogeneous) precipitation at dislocations were also reported by Jones and Humphreys, who investigated different Al-Sc alloys [51], and Somerday and Humphreys for a Al-1.3wt%Mn solid solution [52]. Although the precipitation in both these alloy systems took place by nucleation and growth rather than spinodal decomposition and thus is only partially comparable to that observed in the current study, the strong influence of the deformation substructure on the size of precipitates is consistent. In contrast, Han et al. [53] reported no significant influence of lattice defects on the spinodal decomposition in a Fe-32Mn-8Al-0.9C-0.2Mo steel. However, the quality of TEM micrographs was very poor as compared to current-state TEM investigations.

The precipitation kinetics and morphology of κ-carbides in recrystallized material after annealing at different annealing temperatures and times were investigated in addition to the precipitation of κ-carbides in deformed material. As can be seen in Fig. 3, the hardness increase observed upon annealing of the RX material (dashed lines) decreased with rising annealing temperature. Assuming a similar size of the *intra*granular carbides, this decrease is attributed mainly to the lower volume fraction of κ-carbides precipitating at higher temperatures (due to lower supersaturation at higher temperatures). Further, it is known that with increasing annealing temperature the relative fraction of *inter*granular κ-carbides increases [10]. Since intergranular κ-carbides do not contribute strongly to the age-hardenability, this circumstance provides an additional reason for the lower hardness increase at higher temperatures. Furthermore, it has to be also noticed, that for all annealing temperatures, the major age hardening took place in the first 60 min of annealing. This gives evidence that the precipitation occurs fast, which is in line with several previous studies [3, 4, 40]. Although no direct comparison to the precipitation kinetics in the deformed material can be drawn owing to the very different size and morphology of the respective κ-carbides (as has been discussed already), the obtained knowledge from the RX material is important for the determination of annealing parameters to control the mechanical properties (cf. section 4.3). Based on the findings discussed in this paragraph, low annealing temperatures and short annealing times were proven to be required for an effective age-hardening treatment and suppression of brittle intergranular κ-carbides.

4.2 Recovery and recrystallization behaviour

Typically observed recrystallization hardness curves in single-phase low-SFE HMnS show a hardness plateau at short annealing times and a consequent hardness drop correlating to the recrystallized volume fraction [54, 55]. However, the deformed light-weight HMnS investigated in the current study

revealed an increasing hardness at short annealing times followed by a hardness decrease (to a level slightly below the initial hardness) of the CR material during annealing at temperatures of 600 and 650 °C (cf. Fig. 3). Having in mind that the precipitation of κ-carbides is known to result in a strong age-hardening of light-weight HMnS [12, 35, 36], from all microstructural changes possible during annealing, only the precipitation of κ-carbides can be responsible for the increasing hardness at short annealing times. The presence of these precipitates was, indeed, confirmed by TEM (Fig. 5).

Further, as has been discussed in the previous section and shown by TEM, no significant coarsening of the κ-carbides took place with extended annealing times, which indicated that a hardness decrease was not attributed to overaging. During annealing at 600 °C, the onset of recrystallization was not initiated (see section 3.3. and Fig. 4). We can therefore conclude, that softening of the material was solely caused by static recovery processes. Although the precipitated κ-carbides obviously retard dislocation motion during their rearrangement in the course of recovery, the dislocation activity/mobility in the austenitic matrix still remains sufficiently high facilitate recovery. Recovery in material with coherent precipitates has also been described by Dawson et al. [56]. Although the precipitates were already present in the material before the annealing treatment, their effect on recovery was low. Jones and Humphreys [51] reported on the coarsening and formation of semi-coherent boundaries of previously coherent particles by the passage of low-angle grain boundary during recovery. Similar observations, though, were not made in the current study.

Onset of recrystallization (i.e. recrystallization nuclei) was observed after 240 min annealing at 650 °C, which resulted in a decreasing hardness. The nucleation sites (grain boundaries and triple junctions) were the same as reported e.g. for TWIP steels [55, 57, 58], yet the growth of the nuclei was severely inhibited due to the presence of inter- and intragranular κ-carbides (cf. Fig. 4). During annealing at 700 °C, where the driving force for precipitation was significantly lower due to the decreased supersaturation, and recrystallization was favoured due to enhanced diffusion, recrystallization became more rapid than precipitation, resulting in a partial recrystallization. The progressive precipitation of inter- and intragranular κ-carbides, however, prevented its completion. Full recrystallization could only be achieved by annealing in the austenite single-phase temperature range (Figs. 1 and 2). Consequently, the κ-carbides effectively impeded grain boundary motion by exertion of a pinning-force. In comparison to a single-phase TWIP steel, in which full recrystallization in a 30% cold rolled material was achieved after 300 s at 700 °C [58], the recrystallization kinetics in the investigated light-weight HMnS is, however, strongly retarded. It is also worth noting that light-weight HMnS contain a higher fraction of alloying elements (specifically carbon), which segregate at grain boundaries and result in an additional pinning force [59].

The texture evolution during recrystallization can provide an explanation for the operating mechanisms of recrystallization. The retention but weakening of the deformation texture during recrystallization observed in the current study (Fig. 6), has also been reported for HMnS TWIP steels

[58]. This observation was attributed to oriented nucleation and formation of new orientations by recrystallization twinning. These mechanisms are assumed to be responsible for the texture evolution also in the investigated light-weight HMnS and were clearly not affected by the presence of κ-carbides.

In conclusion, the mutual interaction of precipitation and recrystallization during annealing of the studied light-weight HMnS appears to be quite complex and, depending on the temperature, either one of the processes proceeds more rapid than the other, resulting in complete inhibition or only retardation of recrystallization.

4.3 Deformation behaviour and tailored heat treatment for optimized properties

The impact of precipitation in combination with recovery/recrystallization on hardness gave a first indication for the potential of a combined softening and precipitation-hardening heat treatment. Yet, the hardness does not provide sufficient information to comprehensively evaluate the mechanical properties, such as the investigated tensile behaviour (Fig. 7), which will be discussed in the following.

It was already established that very high yield strength in the light-weight HMnS resulted from the strong work hardening during cold rolling due to dynamic slip band refinement [2-4, 28, 35]. In order to optimize the mechanical properties, i.e. to retain the high yield strength and concurrently improve the ductility, a combination of recovery and intragranular precipitation was aspired in the current study. Now the question is, which parameters of the heat treatment (temperature and annealing time) should be chosen in order to achieve this goal.

For the annealing treatment performed within the temperature range in which κ-carbide precipitation occurs, lower temperatures are desirable, since the relative fraction of intragranular precipitates after annealing at lower temperatures is higher than that of the intergranular precipitates [10] (see section 4.1). In contrast, for recovery higher temperatures are favourable to enhance the dislocation mobility [60]. Annealing at 600 °C for 10 minutes resulted in the very high yield strength ($\sigma_{0.2}$ > 1.4 GPa), similar to that of the deformed material, and substantially improved ductility ($\varepsilon_f \approx 7\%$) (cf. Fig. 7). In this condition, the recovered austenite accounted for an increased ductility, whereas the remaining high dislocation density and intragranular κ-carbides served for a high yield strength. In order to obtain even higher ductility, one would tend to apply a longer annealing time. However, the observed brittle fracture (Fig. 8), which is attributed to the precipitation of coarse intergranular κ-carbides (seen as nodules in the fracture surfaces in Fig. 8) promoting intergranular fracture [37-39], became more pronounced with increasing annealing time. This points to the increase of the intergranular precipitation with time, which in turn has a detrimental effect on the ductility (Fig. 7). This observation is in line with results of several studies performed on recrystallized light-weight HMnS that reported on a gradual decrease in both strength and ductility due to the formation of coarse

intergranular κ-carbides [37-39]. Therefore, the obtained results revealed a high sensitivity of the mechanical behaviour of investigated material against the annealing time, since the time range in which precipitation of intragranular κ-carbides is predominant is fairly short (cf. section 4.1 and [51, 52]).

In order to elucidate whether, and if so, how the improvement in ductility observed in the 50% cold rolled (and then annealed) material depends on the degree of rolling reduction additional experiments were conducted. In these, 30% and 40% cold-rolled material was examined in the cold-rolled and annealed states. The evolution of yield strength and elongation to fracture, ε_f, with annealing time during annealing at 600 °C is presented in Fig. 10 for rolling reductions between 30% and 50% and shows the different impact of combined recovery and precipitation. In the 40 and 50% cold rolled material, whilst the yield strength did not show a strong change, ε_f increased for short annealing times (10 min) and decreased for intermediate annealing times (30 min). The effect was less pronounced in the 40% cold rolled material and even reversed in the 30% cold rolled material, where ε_f was similar in the cold rolled condition and after a short annealing time and increased at intermediate annealing times. The evolution of ε_f reveals the necessity for a precise choice of the applied conditions for recovery and precipitation in order to actually control the mechanical properties. The kinetics of both processes, precipitation and recovery, decrease at lower rolling reductions (due to less pronounced deformation substructure) [51, 52, 61]. Therefore, the increase in ductility and embrittlement by intergranular precipitation at lower rolling reductions is postponed to longer annealing times, making the annealing treatment less sensitive with respect to the annealing time. Overall, the progress and, therefore, interaction of recovery and precipitation processes and the resulting mechanical properties are affected by the characteristic of the deformation substructure. The degree of pre-deformation can therefore be effectively utilized to achieve a wide range of properties. Summarizing, a more pronounced deformation substructure leads to a more rapid precipitation and recovery and relatively higher improvements in ε_f. However, the process becomes more sensitive against the annealing time, since, as observed in the studied alloy, the precipitation of intergranular κ-carbides can only be prevented by applying shorter annealing times.

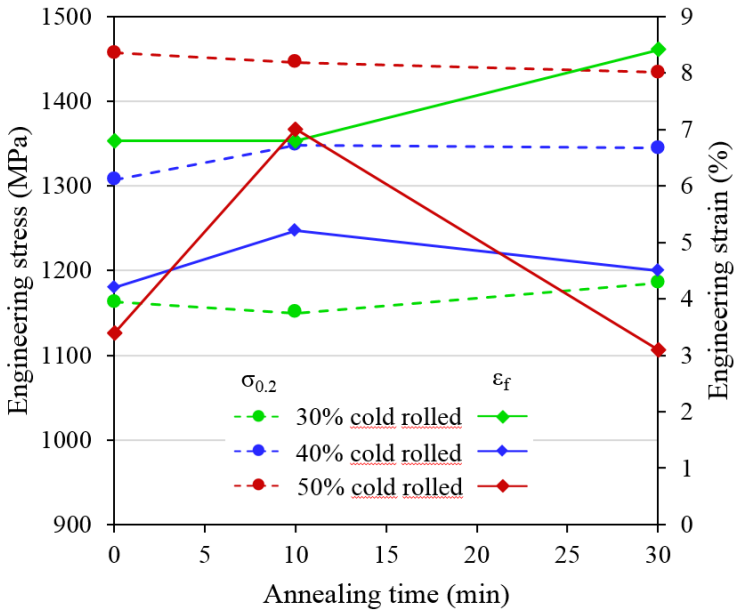

Fig. 10. Evolution of yield strength ($\sigma_{0.2}$) and elongation to fracture (ε_f) with annealing time for material rolled to 30, 40 and 50% thickness reduction.

5. Summary

In the present study, the precipitation behaviour of a Fe-29.8Mn-7.65Al-1.11C light-weight steel with distinct deformation substructure and the interplay between κ-carbide precipitation and recovery and/or recrystallization processes, i.e. concurrent strengthening and softening, were investigated. The steel was age-hardened (in the temperature range between 600 °C and 800 °C) in the deformed/cold rolled and recrystallized states, in order to elucidate the influence of the initial microstructure on κ-carbide precipitation and the resulting mechanical properties. The gained knowledge was utilized to design a thermo-mechanical treatment with the aid of improving the mechanical properties. Following conclusions can be drawn:

- The deformation substructure in the deformed material strongly affected the precipitation of intragranular κ-carbides. The κ-carbides precipitated preferentially at defects and were significantly larger, as compared to κ-carbides formed in the recrystallized material. This difference can be attributed to faster diffusion of solutes (along dislocation cores, i.e. pipe diffusion) in the deformed material, which enabled spinodal decomposition to occur in a larger spatial volume. Albeit the increased size, fully coherent κ/γ phase boundaries were observed implying that further growth of the κ-carbides was restricted by coherency strains.
- In the recrystallized material the age-hardening potential decreased with increasing temperature, due to the lower supersaturation and lower relative fraction of intragranular κ-carbides at higher temperatures. Since the major hardness increase occurred in the first 60 min of annealing, the precipitation is assumed to occur fast. Therefore, effective age hardening is achieved at relatively low annealing temperatures and short annealing times.

- During annealing of the deformed material at 600 °C, static recovery processes (no recrystallization was observed at this temperature) facilitated regained ductility combined with high retained hardness and strength. Concurrent precipitation of κ-carbides restricted dislocation mobility only partially. Hence, dislocation rearrangement and annihilation remained sufficiently high to enable static recovery.
- At elevated temperatures (650-700 °C), the lower supersaturation of the fcc phase and increased diffusivity resulted in the formation of recrystallization nuclei. Their growth, however, was strongly inhibited by the progressive precipitation of κ-carbides and segregation of alloying elements at the grain boundaries, which both were shown to effectively pin grain boundaries and prohibit complete recrystallization. Full recrystallization was only achieved during annealing in the single-phase austenitic temperature region (above 770 °C).
- Controlling the microstructure via combined pre-deformation (cold rolling) with varying rolling degrees and annealing to promote κ-carbide precipitation, recovery and/or recrystallization allows for tailoring the mechanical properties in a wide range. Short annealing (e.g. 10 min) at low temperature (600 °C) enabled ultra-high strength combined with regained ductility due to concurrent intragranular κ-carbide precipitation, recovery and suppression of brittle intergranular κ-carbides.

Acknowledgements

The authors express their special thanks to the financial support of the Deutsche Forschungsgemeinschaft (DFG) within the Collaborative Research Center (SFB) 761 “Steel – ab initio; quantum mechanics guided design of new Fe based materials”.

Conflict of Interest

The authors declare no conflict of interest.

Data Availability

The raw data required to reproduce these findings cannot be shared at this time as the data also forms part of an ongoing study. The processed data required to reproduce these findings cannot be shared at this time due to legal or ethical reasons.

References

[1] D. Liu, M. Cai, H. Ding and D. Han, Control of inter/intra-granular κ -carbides and its influence on overall mechanical properties of a Fe-11Mn-10Al-1.25C low density steel. Materials Science and Engineering: A. 715 (2018) 25-32. DOI: 10.1016/j.msea.2017.12.102.

[2] C. Haase, C. Zehnder, T. Ingendahl, A. Bikar, F. Tang, B. Hallstedt, W. Hu, W. Bleck and D.A. Molodov, On the deformation behavior of κ-carbide-free and κ-carbide-containing high-

Mn light-weight steel. Acta Materialia. 122 (2017) 332-343. DOI: 10.1016/j.actamat.2016.10.006.
[3] M.J. Yao, E. Welsch, D. Ponge, S.M.H. Haghighat, S. Sandlöbes, P. Choi, M. Herbig, I. Bleskov, T. Hickel, M. Lipinska-Chwalek, P. Shanthraj, C. Scheu, S. Zaefferer, B. Gault, and D. Raabe, Strengthening and strain hardening mechanisms in a precipitation-hardened high-Mn lightweight steel. Acta Materialia. 140 (2017) 258-273. DOI: 10.1016/j.actamat.2017.08.049.
[4] E. Welsch, D. Ponge, S.M. Hafez Haghighat, S. Sandlöbes, P. Choi, M. Herbig, S. Zaefferer and D. Raabe, Strain hardening by dynamic slip band refinement in a high-Mn lightweight steel. Acta Materialia. 116 (2016) 188-199. DOI: 10.1016/j.actamat.2016.06.037.
[5] H. Kim, D.W. Suh and N.J. Kim, Fe-Al-Mn-C lightweight structural alloys: a review on the microstructures and mechanical properties. Sci Technol Adv Mater. 14 (2013) 014205. DOI: 10.1088/1468-6996/14/1/014205.
[6] M.T. Jahn, S.C. Chang and Y.H. Hsiao, Transverse tensile and fatigue properties of Fe-Mn-Al-C alloys. Journal of Materials Science Letters. 8 (1989) 723-724. DOI: 10.1007/BF01730455.
[7] I.S. Kalashnikov, O. Acselrad, T. Kalichak, M.S. Khadyyev and L.C. Pereira, Behavior of Fe-Mn-Al-C steels during cyclic tests. Journal of Materials Engineering and Performance. 9 (2000) 334-337. DOI: 10.1361/105994900770346015.
[8] P.R.S. Jackson and G.R. Wallwork, High temperature oxidation of iron-manganese-aluminum based alloys. Oxidation of Metals. 21 (1984) 135-170. DOI: 10.1007/BF00741468.
[9] C.H. Kao and C.M. Wan, Effect of temperature on the oxidation of Fe-7.5A1-o.65C alloy. Journal of Materials Science. 23 (1988) 1943-1947. DOI: 10.1007/BF01115754.
[10] M.C. Li, H. Chang, P.W. Kao and D. Gan, The effect of Mn and Al contents on the solvus of κ phase in austenitic Fe-Mn-Al-C alloys. Materials Chemistry and Physics. 59 (1999) 96-99. DOI: https://doi.org/10.1016/S0254-0584(99)00026-7.
[11] H. Huang, D. Gan and P.W. Kao, Effect of alloying additions on the κ phase precipitation in austenitic Fe-Mn-Al-C alloys. Scripta Metallurgica et Materialia. 30 (1994) 499-504. DOI: https://doi.org/10.1016/0956-716X(94)90610-6.
[12] G. Frommeyer and U. Brüx, Microstructures and mechanical properties of high strength Fe-Mn-Al-C light-weight TRIPLEX steels. Steel Research International. 77 (2006) 627-633.
[13] K.H. Han, J.C. Yoon and W.K. Choo, TEM evidence of modulated structure in F-Mn-Al-C austenitic alloys. Scripta Metallurgica. 20 (1986) 33-36. DOI: https://doi.org/10.1016/0036-9748(86)90208-5.
[14] K. Sato, K. Tagawa and Y. Inoue, Age hardening of an Fe-30Mn-9Al-0.9C alloy by spinodal decomposition. Scripta Metallurgica. 22 (1988) 899-902. DOI: https://doi.org/10.1016/S0036-9748(88)80071-1.
[15] M.J. Yao, P. Dey, J.B. Seol, P. Choi, M. Herbig, R.K.W. Marceau, T. Hickel, J. Neugebauer and D. Raabe, Combined atom probe tomography and density functional theory investigation of the Al off-stoichiometry of κ-carbides in an austenitic Fe–Mn–Al–C low density steel. Acta Materialia. 106 (2016) 229-238. DOI: 10.1016/j.actamat.2016.01.007.
[16] O. Acselrad, I.S. Kalashnikov, E.M. Silva, M.S. Khadyev and R.A. Simao, Diagram of phase transformation in the austenite of hardened alloy Fe-28%Mn-8.5%Al-1%C-1.25%Si as a result of aging due to isothermal heating. Metal Science and Heat Treatment. 48 (2006) 543-553.
[17] K. Sato, K. Tagawa and Y. Inoue, Spinodal decomposition and mechanical properties of an austenitic Fe-30wt.%Mn-9wt.%Al-0.9wt.%C alloy. Materials Science and Engineering: A. 111 (1989) 45-50. DOI: https://doi.org/10.1016/0921-5093(89)90196-2.
[18] W.-C. Cheng, C.-Y. Cheng, C.-W. Hsu and D.E. Laughlin, Phase transformation of the L1 2 phase to kappa-carbide after spinodal decomposition and ordering in an Fe–C–Mn–Al austenitic steel. Materials Science and Engineering: A. 642 (2015) 128-135. DOI: 10.1016/j.msea.2015.06.096.
[19] K.H. Han and W.K. Choo, Phase decomposition of rapidly solidified Fe-Mn-Al-C austenitic alloys. Metallurgical Transactions A. 20 (1989) 205-214. DOI: 10.1007/BF02670246.
[20] K. Sato, K. Tagawa and Y. Inoue, Modulated structure and magnetic properties of age-hardenable FE-Mn-Al-C alloys. Metallurgical Transactions A. 21A (1990) 5-11.

[21] L.N. Bartlett, D.C. Van Aken, J. Medvedeva, D. Isheim, N.I. Medvedeva and K. Song, An Atom Probe Study of Kappa Carbide Precipitation and the Effect of Silicon Addition. Metallurgical and Materials Transactions A. 45 (2014) 2421-2435. DOI: 10.1007/s11661-014-2187-3.
[22] S. Chen, R. Rana, A. Haldar and R.K. Ray, Current state of Fe-Mn-Al-C low density steels. Progress in Materials Science. 89 (2017) 345-391. DOI: 10.1016/j.pmatsci.2017.05.002.
[23] R. Rana, C. Liu and R.K. Ray, Evolution of microstructure and mechanical properties during thermomechanical processing of a low-density multiphase steel for automotive application. Acta Materialia. 75 (2014) 227-245. DOI: 10.1016/j.actamat.2014.04.031.
[24] J. Jeong, C.-Y. Lee, I.-J. Park and Y.-K. Lee, Isothermal precipitation behavior of κ-carbide in the Fe–9Mn–6Al–0.15C lightweight steel with a multiphase microstructure. Journal of Alloys and Compounds. 574 (2013) 299-304. DOI: 10.1016/j.jallcom.2013.05.138.
[25] C.-H. Seo, K.H. Kwon, K. Choi, K.-H. Kim, J.H. Kwak, S. Lee and N.J. Kim, Deformation behavior of ferrite–austenite duplex lightweight Fe–Mn–Al–C steel. Scripta Materialia. 66 (2012) 519-522. DOI: 10.1016/j.scriptamat.2011.12.026.
[26] B.C. De Cooman, K.-G. Chin and J. Kim, *High Mn TWIP steels for automotive applications*, in *New Trends and Developments in Automotive System Engineering*, P.M. Chiaberge, Editor. 2011, InTech.
[27] J. Yoo and K.-T. Park, Microband-induced plasticity in a high Mn–Al–C light steel. Materials Science and Engineering: A. 49 (2008) 417-424.
[28] I. Gutierrez-Urrutia and D. Raabe, Influence of Al content and precipitation state on the mechanical behavior of austenitic high-Mn low-density steels. Scripta Materialia. 68 (2013) 343-347. DOI: 10.1016/j.scriptamat.2012.08.038.
[29] K.-T. Park, Tensile deformation of low-density Fe–Mn–Al–C austenitic steels at ambient temperature. Scripta Materialia. 68 (2013) 375-379. DOI: 10.1016/j.scriptamat.2012.09.031.
[30] S.D. Kim, J.Y. Park, S.J. Park, J.H. Jang, J. Moon, H.Y. Ha, C.H. Lee, J.Y. Kang, J.H. Shin and T.H. Lee, Direct observation of dislocation plasticity in high-Mn lightweight steel by in-situ TEM. Sci Rep. 9 (2019) 15171. DOI: 10.1038/s41598-019-51586-y.
[31] V. Gerold and H.P. Karnthaler, On the origin of planar slip in f.c.c. alloys. Acta Metallurgica. 37 (1989) 2177-2183. DOI: https://doi.org/10.1016/0001-6160(89)90143-0.
[32] S.I. Hong and C. Laird, Mechanisms of slip mode modification in F.C.C. solid solutions. Acta Metallurgica et Materialia. 38 (1990) 1581-1594. DOI: https://doi.org/10.1016/0956-7151(90)90126-2.
[33] D.A. Hughes, Microstructural evolution in a non-cell forming metal: Al□Mg. Acta Metallurgica et Materialia. 41 (1993) 1421-1430. DOI: https://doi.org/10.1016/0956-7151(93)90251-M.
[34] K. Choi, C.-H. Seo, H. Lee, S.K. Kim, J.H. Kwak, K.G. Chin, K.-T. Park and N.J. Kim, Effect of aging on the microstructure and deformation behavior of austenite base lightweight Fe–28Mn–9Al–0.8C steel. Scripta Materialia. 63 (2010) 1028-1031. DOI: 10.1016/j.scriptamat.2010.07.036.
[35] D. Raabe, H. Springer, I. Gutierrez-Urrutia, F. Roters, M. Bausch, J.B. Seol, M. Koyama, P.P. Choi and K. Tsuzaki, Alloy Design, Combinatorial Synthesis, and Microstructure–Property Relations for Low-Density Fe-Mn-Al-C Austenitic Steels. Jom. 66 (2014) 1845-1856. DOI: 10.1007/s11837-014-1032-x.
[36] H. Springer and D. Raabe, Rapid alloy prototyping: Compositional and thermo-mechanical high throughput bulk combinatorial design of structural materials based on the example of 30Mn–1.2C–xAl triplex steels. Acta Materialia. 60 (2012) 4950-4959. DOI: 10.1016/j.actamat.2012.05.017.
[37] K.M. Chang, C.G. Chao and T.F. Liu, Excellent combination of strength and ductility in an Fe–9Al–28Mn–1.8C alloy. Scripta Materialia. 63 (2010) 162-165. DOI: 10.1016/j.scriptamat.2010.03.038.
[38] C.L. Lin, C.G. Chao, H.Y. Bor and T.F. Liu, Relationship between Microstructures and Tensile Properties of an Fe-30Mn-8.5Al-2.0C Alloy. Materials Transactions. 51 (2010) 1084-1088. DOI: 10.2320/matertrans.M2010013.
[39] W.K. Choo, J.H. Kim and J.C. Yoon, Microstructural change in austenitic Fe-30.0wt%Mn-7.8wt%Al-1.3wt%C initiated by spinodal decomposition and its influence on mechanical

properties. Acta Materialia. 45 (1997) 4877-4885. DOI: https://doi.org/10.1016/S1359-6454(97)00201-2.
[40] W. Song, W. Zhang, J. von Appen, R. Dronskowski and W. Bleck, κ-Phase Formation in Fe-Mn-Al-C Austenitic Steels. Steel Research International. 86 (2015) 1161-1169. DOI: 10.1002/srin.201400587.
[41] A. Saeed-Akbari, J. Imlau, U. Prahl and W. Bleck, Derivation and Variation in Composition-Dependent Stacking Fault Energy Maps Based on Subregular Solution Model in High-Manganese Steels. Metallurgical and Materials Transactions A. 40 (2009) 3076-3090. DOI: 10.1007/s11661-009-0050-8.
[42] A. Saeed-Akbari, L. Mosecker, A. Schwedt and W. Bleck, Characterization and prediction of flow behavior in high-manganese twinning induced plasticity steels: Part I. Mechanism maps and work-hardening behavior. Metallurgical and Materials Transactions A. 43 (2011) 1688-1704. DOI: 10.1007/s11661-011-0993-4.
[43] M. Luysberg, M. Heggen and K. Tillmann, FEI Tecnai G2 F20. Journal of Large-Scale Research Facilities. 2 (2016) A77. DOI: http://dx.doi.org/10.17815/jlsrf-2-138.
[44] A. Kovács, R. Schierholz and K. Tillmann, FEI Titan G2 80-200 CREWLEY. Journal of Large-Scale Research Facilities. 2 (2016) A43. DOI: http://dx.doi.org/10.17815/jlsrf-2-68.
[45] R. Hielscher and H. Schaeben, A novel pole figure inversion method: specification of the MTEX algorithm. Journal of Applied Crystallography. 41 (2008) 1024-1037. DOI: 10.1107/s0021889808030112.
[46] F. Bachmann, R. Hielscher and H. Schaeben, Texture analysis with MTEX – Free and open source software toolbox. Solid State Phenomena. 160 (2010) 63-68. DOI: 10.4028/www.scientific.net/SSP.160.63.
[47] A.A. Saleh, E.V. Pereloma and A.A. Gazder, Texture evolution of cold rolled and annealed Fe–24Mn–3Al–2Si–1Ni–0.06C TWIP steel. Materials Science and Engineering: A. 528 (2011) 4537-4549. DOI: 10.1016/j.msea.2011.02.055.
[48] P. Dey, R. Nazarov, B. Dutta, M. Yao, M. Herbig, M. Friák, T. Hickel, D. Raabe and J. Neugebauer, Ab initio explanation of disorder and off-stoichiometry in Fe-Mn-Al-C κ-carbides. Physical Review B. 95 (2017). DOI: 10.1103/PhysRevB.95.104108.
[49] M.J. Yao, *κ-carbide in a high-Mn light-weight steel: precipitation, off-stoichiometry and deformation*, in *Faculty of Georesources and Materials Engineering*. 2017, RWTH Aachen University: Aachen.
[50] M. Legros, G. Dehm, E. Arzt and T.J. Balk, Observation of Giant Diffusivity Along Dislocation Cores. Science. 319 (2008) 1646. DOI: 10.1126/science.1151771.
[51] M.J. Jones and F.J. Humphreys, Interaction of recrystallization and precipitation: The effect of Al3Sc on the recrystallization behaviour of deformed aluminium. Acta Materialia. 51 (2003) 2149-2159. DOI: 10.1016/s1359-6454(03)00002-8.
[52] M. Somerday and F.J. Humphreys, Recrystallisation behaviour of supersaturated Al–Mn alloys Part 1 – Al–1.3 wt-%Mn. Materials Science and Technology. 19 (2003) 20-29. DOI: 10.1179/026708303225008590.
[53] K.H. Han, T.S. Kang and D.E. Laughlin. *Thermomechanical treatment of FeMnAlC sideband alloy*. in *Precipitation Phenomena: Deformation and Aging*. 1988. Chicago, USA.
[54] C. Haase, L.A. Barrales-Mora, D.A. Molodov and G. Gottstein, Texture evolution of a cold-rolled Fe-28Mn-0.28C TWIP steel during recrystallization. Materials Science Forum. 753 (2013) 213-216.
[55] Y. Lü, D.A. Molodov and G. Gottstein, Recrystallization kinetics and microstructure evolution during annealing of a cold-rolled Fe–Mn–C alloy. Acta Materialia. 59 (2011) 3229-3243. DOI: 10.1016/j.actamat.2011.01.063.
[56] K. Dawson, A. Rao, G.J. Tatlock and A.R. Jones, Recovery and recrystallisation in mechanically alloyed and annealed, legacy, FeCrAlY ODS alloy precursor powders. IOP Conference Series: Materials Science and Engineering. 89 (2015) 012020. DOI: 10.1088/1757-899x/89/1/012020.
[57] C. Haase, L.A. Barrales-Mora, D.A. Molodov and G. Gottstein, Tailoring the mechanical properties of a twinning-induced plasticity steel by retention of deformation twins during heat treatment. Metallurgical and Materials Transactions A. 44 (2013) 4445-4449. DOI: 10.1007/s11661-013-1935-0.

[58] C. Haase, M. Kühbach, L.A. Barrales-Mora, S.L. Wong, F. Roters, D.A. Molodov and G. Gottstein, Recrystallization behavior of a high-manganese steel: Experiments and simulations. Acta Materialia. 100 (2015) 155-168. DOI: 10.1016/j.actamat.2015.08.057.
[59] M. Herbig, M. Kuzmina, C. Haase, R.K.W. Marceau, I. Gutierrez-Urrutia, D. Haley, D.A. Molodov, P. Choi and D. Raabe, Grain boundary segregation in Fe–Mn–C twinning-induced plasticity steels studied by correlative electron backscatter diffraction and atom probe tomography. Acta Materialia. 83 (2015) 37-47. DOI: 10.1016/j.actamat.2014.09.041.
[60] D. Hull and D.J. Bacon, *Chapter 5 - Dislocations in Face-centered Cubic Metals*, in *Introduction to Dislocations (Fifth Edition)*, D. Hull and D.J. Bacon, Editors. 2011, Butterworth-Heinemann: Oxford. p. 85-107.
[61] F.J. Humphreys and M. Hatherly, *Chapter 6 - Recovery After Deformation*, in *Recrystallization and Related Annealing Phenomena (Second Edition)*, F.J. Humphreys and M. Hatherly, Editors. 2004, Elsevier: Oxford. p. 169-213.

Figure(s)

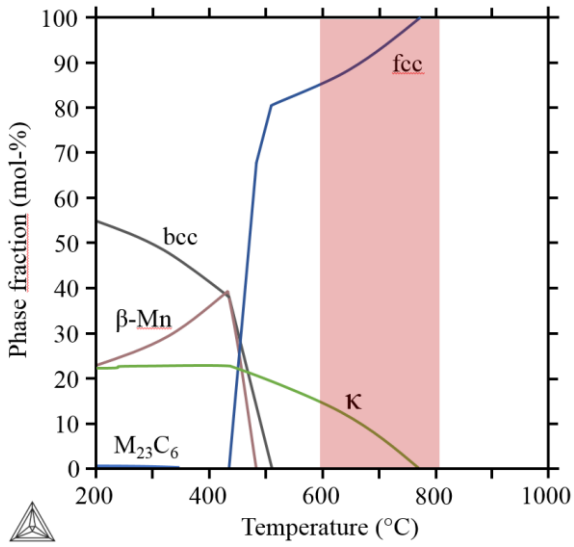

Fig. 1. Equilibrium phase fractions as a function of temperature for the investigated steel (based on [2]). The temperature range in which the final heat treatment was carried out is marked in red.

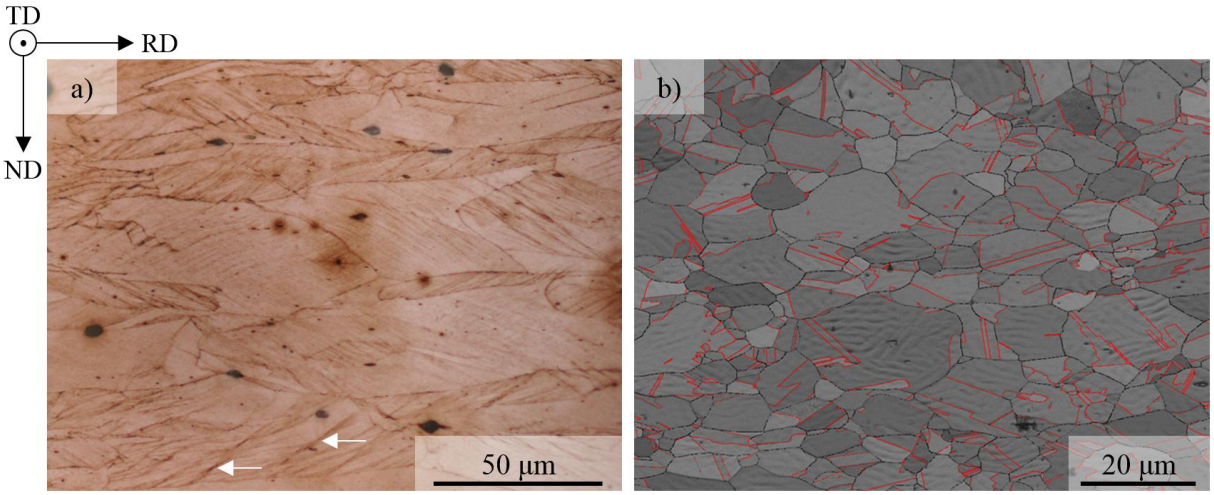

Fig. 2. Micropgraphs of the two initial conditions: a) LOM micrograph of the CR material and b) EBSD band-contrast mapping of the RX material. Red lines denote Σ3 (60°<111>) grain boundaries, white arrows indicate shear bands.

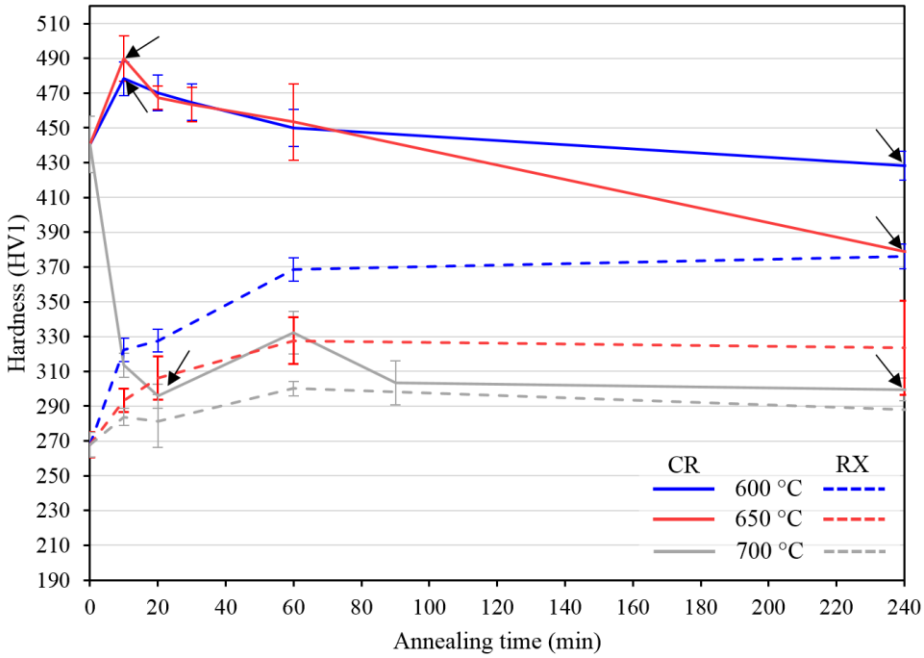

Fig. 3. Hardness evolution as a function of annealing time for the material in the two initial conditions CR (solid lines) and RX (dashed lines) annealed at 600, 650 and 700 °C. The material states investigated in detail in the following paragraphs are marked with black arrows. The corresponding micrographs are illustrated in Figs. 4 and 5).

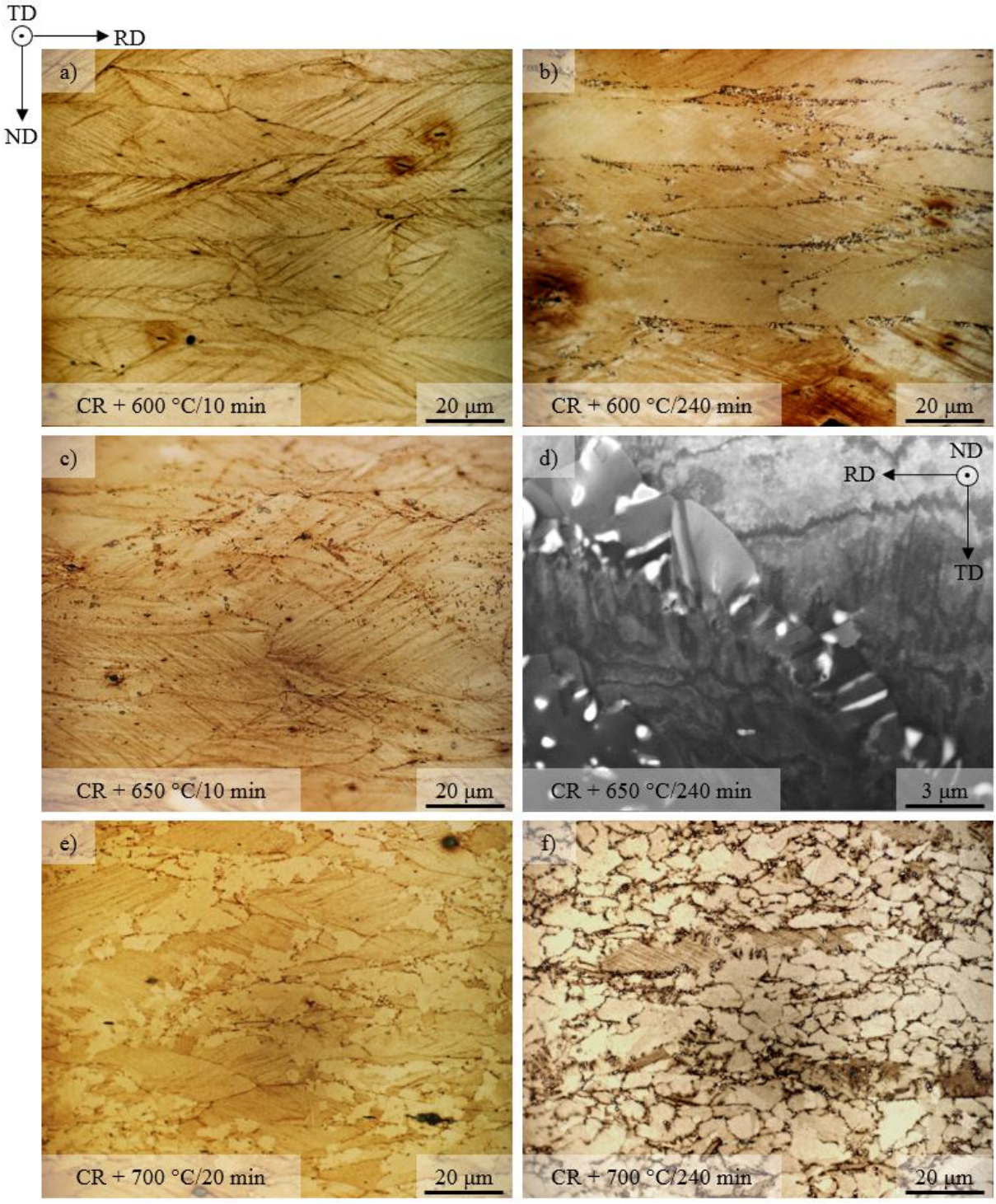

Fig. 4. LOM (a-c, e, f) and STEM (d) micrographs of the CR material annealed at 600 (a, b), 650 (c, d), and 700 °C (e, f). Images of the microstructures obtained after short annealing times of 10 or 20 min are presented in the left column, whereas those obtained after a long annealing time of 240 min are shown in the right column. Note the difference in the relative orientation of the specimens in a, b, c, e and f (the same for all LOM images) and d (STEM) micrograph.

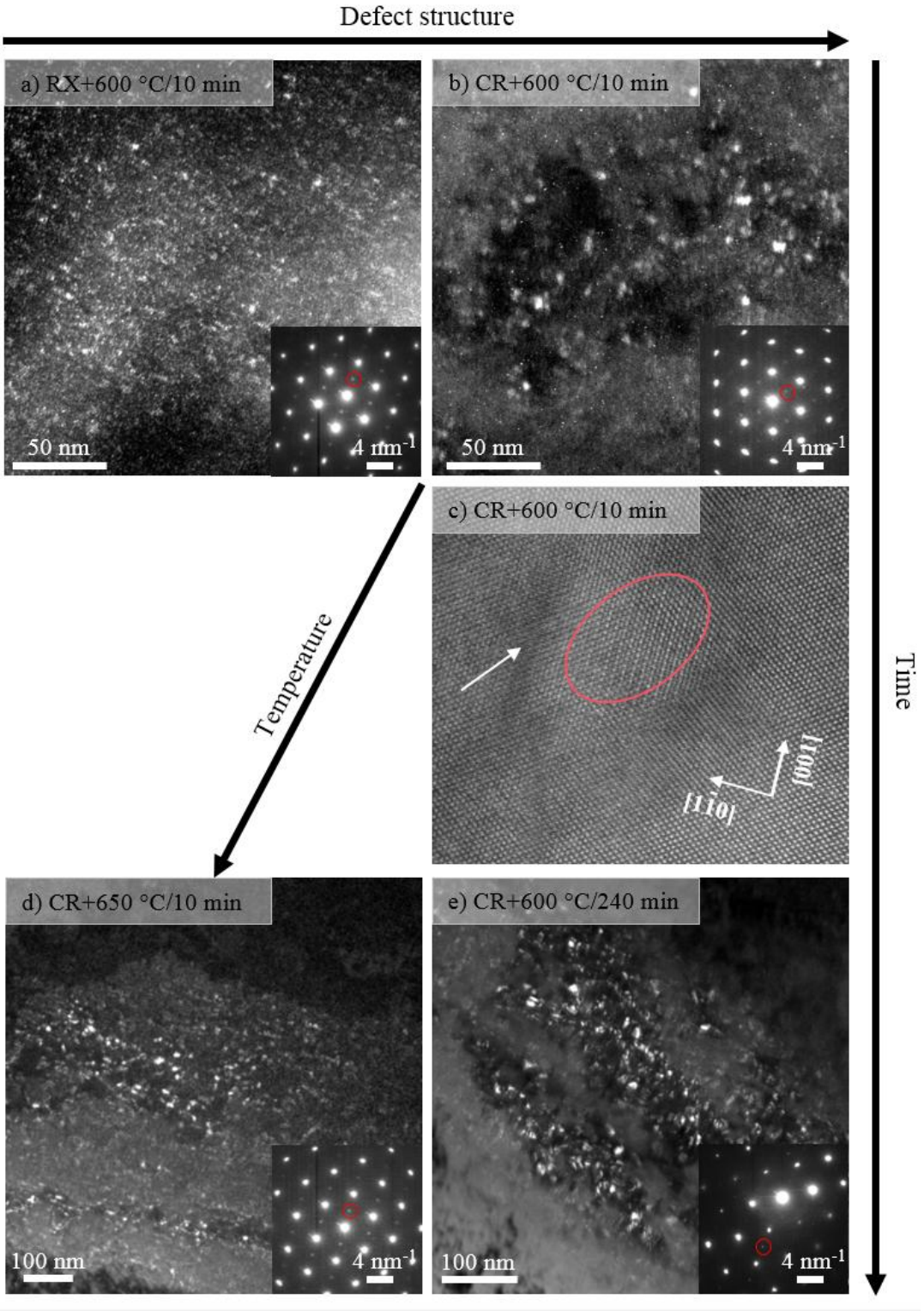

Fig. 5. TEM images of the microstructures observed in RX (a) and CR (b-d) material after annealing treatments at 600 °C for 10 min (a-c), 650 °C for 10 min (d) and 600 °C for 240 min (e). DF TEM images (a, b, d and e) and the corresponding SADPs (insets) acquired in the orientations close to [110] zone axis. Intensities of DF images correspond to the κ-phase super lattice reflections g_κ=(001) in (a-d) and g_κ=(003) in (e), indicated in SADPs with red circles. HR HAADF STEM (c) acquired in the [110] zone axis orientation: red ellipse - encloses κ-carbide precipitate, localized in the vicinity of defects (blurry shadows indicated with white arrow), inset with white vectors - depicts crystallographic directions in the HR image.

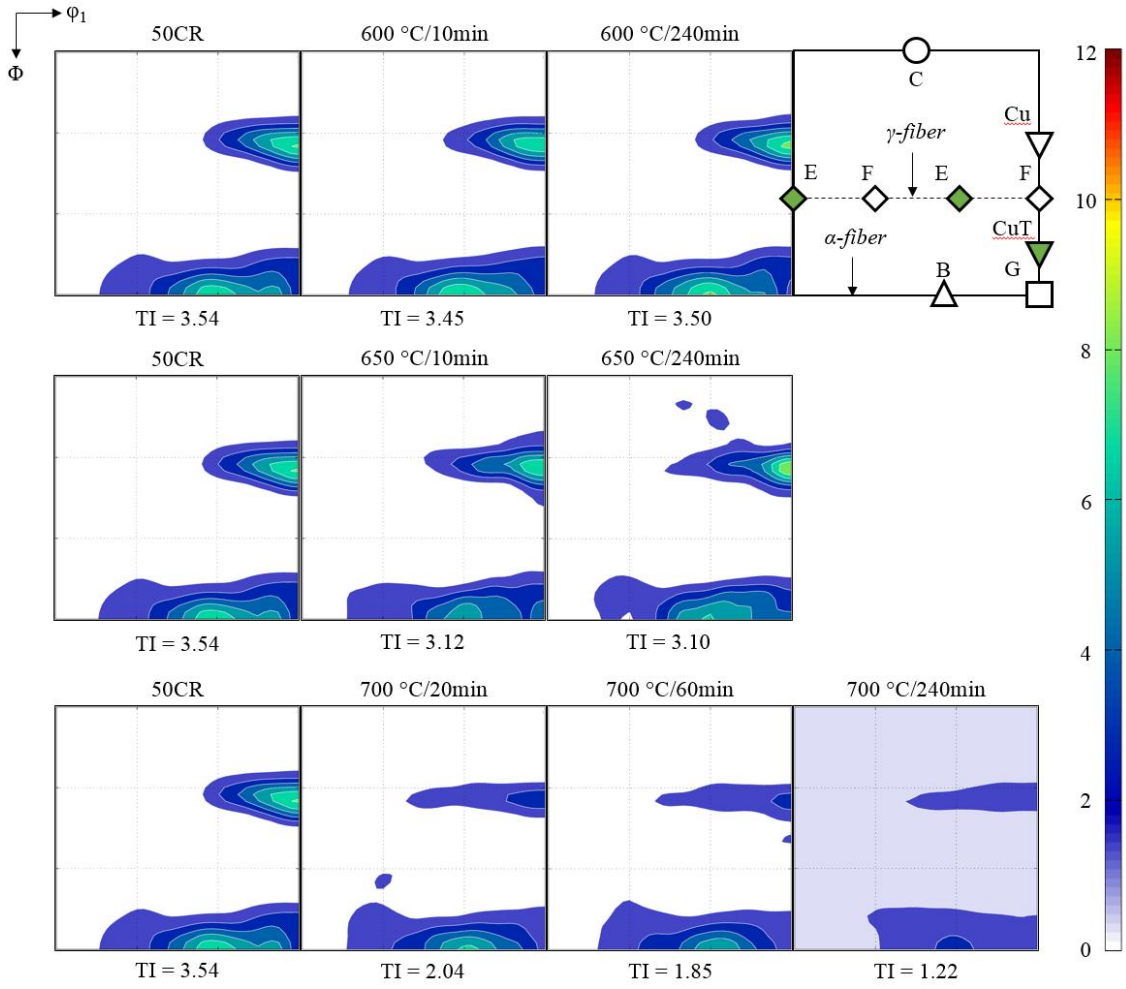

Fig. 6. Texture (ODF sections at φ2=45°) of the CR material annealed at 600 °C and 650 °C for 10 and 240 min, as well as annealed at 700 °C for 20, 60, and 240 min. A schematic of the ideal positions of the rolling texture components is illustrated in the upper right corner. The corresponding declaration of the texture components can be found in Ref. [47].

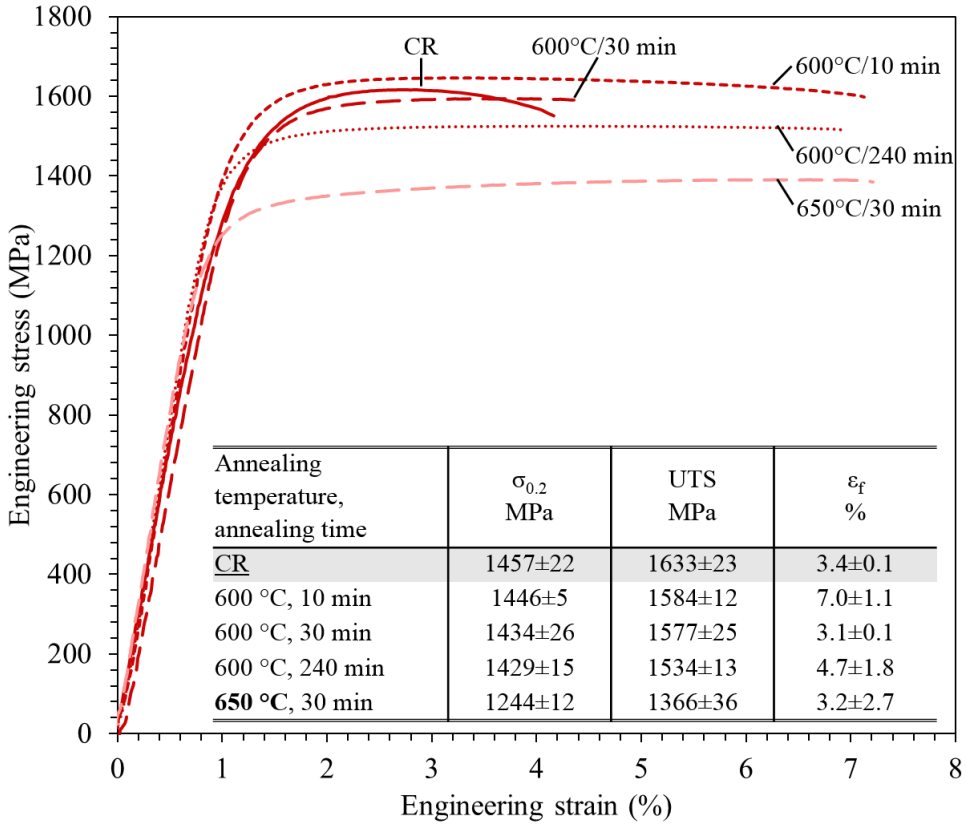

Annealing temperature, annealing time	$\sigma_{0.2}$ MPa	UTS MPa	ε_f %
CR	1457±22	1633±23	3.4±0.1
600 °C, 10 min	1446±5	1584±12	7.0±1.1
600 °C, 30 min	1434±26	1577±25	3.1±0.1
600 °C, 240 min	1429±15	1534±13	4.7±1.8
650 °C, 30 min	1244±12	1366±36	3.2±2.7

Fig. 7. Engineering stress – engineering strain curves and mechanical properties of the investigated material cold rolled to 50% thickness reduction and annealed at 600 and 650 °C for various annealing times.

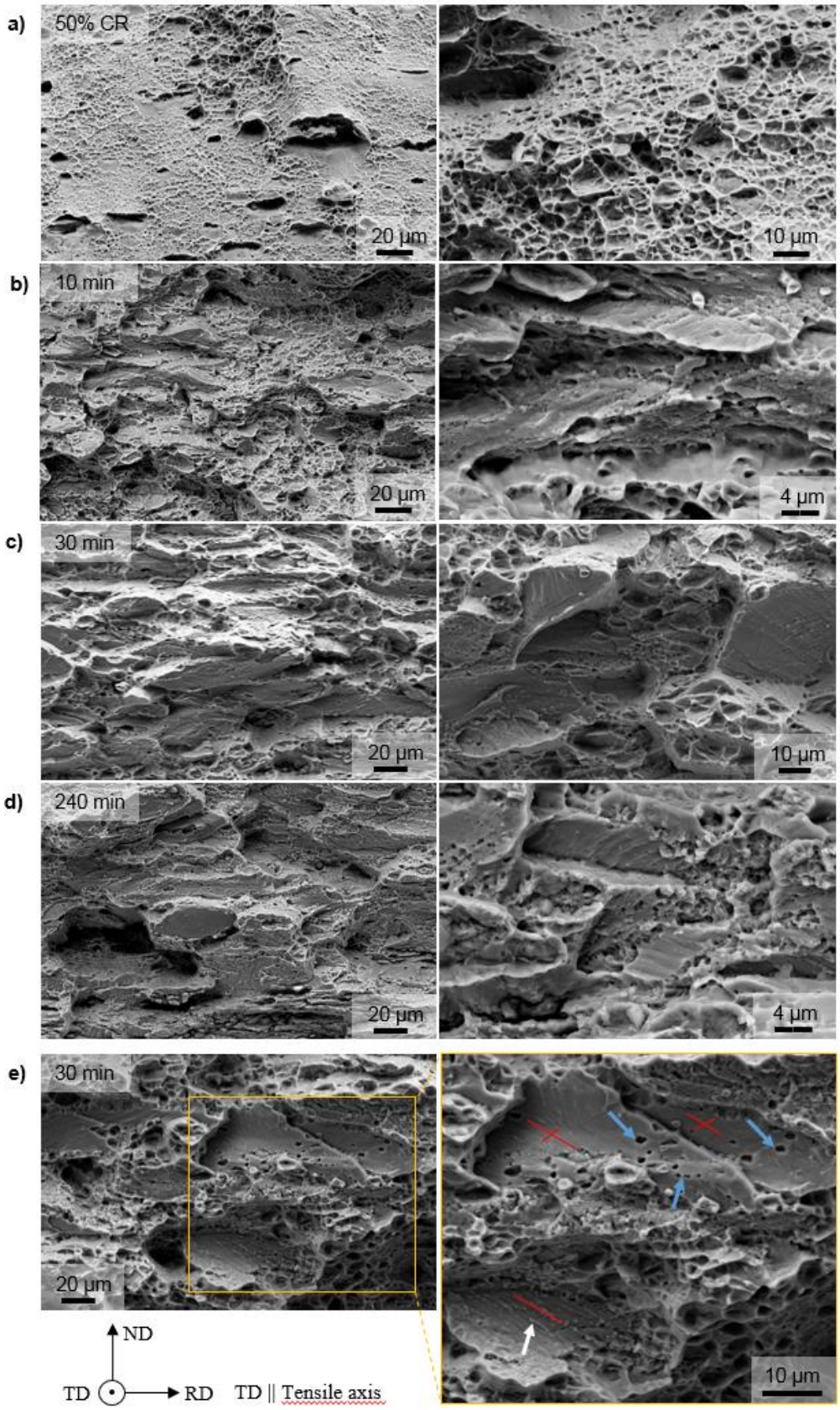

Fig. 8. SE images of the fracture surfaces of tensile test specimens of the CR material in the initial state (a) and after various annealing times at 600 °C (b-d) and 650 °C (e). Images in the left column give an overview of the fracture surface, whereas images in the right column provide a magnified view. In the inset of e) characteristic features on facets found in the materials fracture surfaces are highlighted. Blue arrow: spherical voids, red lines: linear markings, white arrow: nodules.

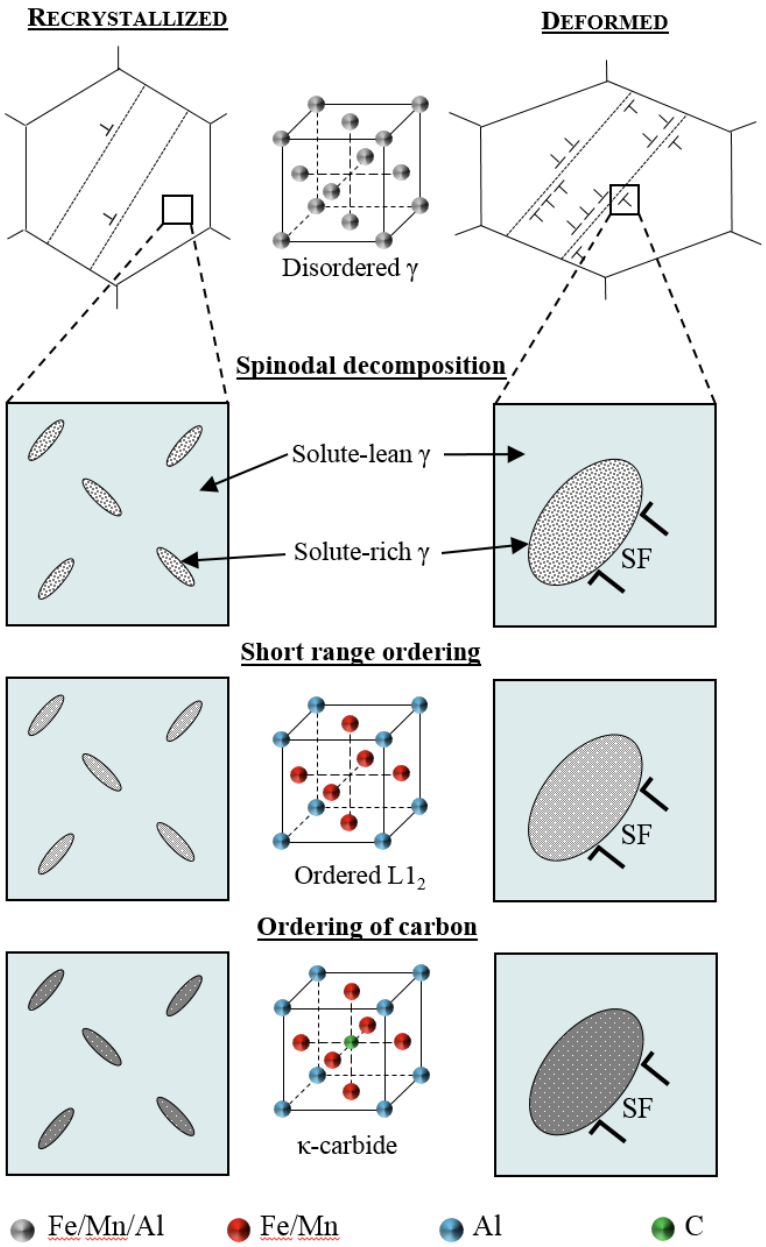

Fig. 9. Schematic of the precipitation mechanism of κ-carbides in recrystallized (left column) and deformed material (right column). SF denotes a stacking fault.

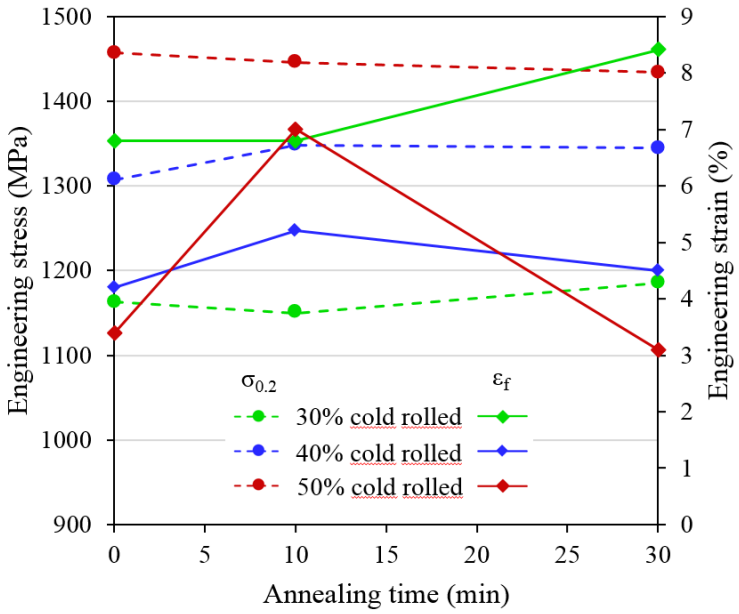

Fig. 10. Evolution of yield strength ($\sigma_{0.2}$) and elongation to fracture (ε_f) with annealing time for material rolled to 30, 40 and 50% thickness reduction.

Table(s)

Table 1. Chemical composition and stacking fault energy value of the investigated steel.

Element	Fe	C	Mn	Al	Si	SFE (mJ/m^2)
(wt%)	bal.	1.11	29.8	7.65	0.09	85

***Declaration of Interest Statement**

Declaration of interests

☒ The authors declare that they have no known competing financial interests or personal relationships that could have appeared to influence the work reported in this paper.

☐The authors declare the following financial interests/personal relationships which may be considered as potential competing interests: